

Understanding mesoscale aggregation of shallow cumulus convection using large-eddy simulation

C. S. Bretherton¹ and P. N. Blossey¹

¹Department of Atmospheric Sciences, University of Washington, Seattle, Washington, USA

Key Points:

- In large-domain LES of shallow cumulus convection, mesoscale moist patches containing clusters of vigorous cumuli develop within 1-2 days.
- The moisture aggregation is analyzed with the weak temperature gradient approximation and mesoscale moisture budgets.
- Gross moist instability drives aggregation even without precipitation and with horizontally uniform radiative and surface fluxes.

Abstract

Marine shallow cumulus convection, often mixed with thin stratocumulus, is commonly aggregated into mesoscale patches. The mechanism and conditions supporting this aggregation are elucidated using 36-hour large-eddy simulations (LES) on a 128×128 km doubly-periodic domain, using climatological summertime forcings for a location southeast of Hawaii. Within 12 hours, mesoscale patches of higher humidity, more vigorous cumulus convection, and thin detrained cloud at the trade inversion base develop spontaneously.

Mesoscale 16×16 km subdomains are composited into quartiles of column total water path and their heat and moisture budgets analyzed. The weak temperature gradient approximation is used to explain how apparent heating perturbations drive simulated mesoscale circulations, which in turn induce relative moistening of the moistest subdomains, a form of gross moist instability.

Self-aggregation is affected by precipitation and mesoscale feedbacks of radiative and surface fluxes, but still occurs without them. In that minimal-physics setting, the humidity budget analysis suggests self-aggregation is more likely if horizontal-mean humidity is a concave function of the horizontal-mean virtual potential temperature, a condition favored by radiative cooling and cold advection within the boundary layer.

1 Introduction

Fig. 1 shows a microwave retrieval of column water vapor path overlaid on a visible image centered at 17°N , 149°W , from the NASA A-Train satellite constellation on July 14, 2015. This location is toward the downstream edge of the climatological stratocumulus (Sc) to shallow cumulus (Cu) transition over the subtropical northeast Pacific ocean. Fig. 1 shows a typical example of the summertime cloud organization at this location, mesoscale clusters of Cu 2-3 km deep rising into surrounding patches of thin Sc. There is also mesoscale variability in the column water vapor path, and the cumulus clusters tend to lie within moist patches. We refer to this as an ‘aggregated’ state of humidity and cumulus convection, since one could imagine a much more homogeneous distribution of these quantities on the mesoscale. This paper aims to develop an improved understanding of how feedbacks between humidity, shallow cumulus convection and related processes may promote this aggregation.

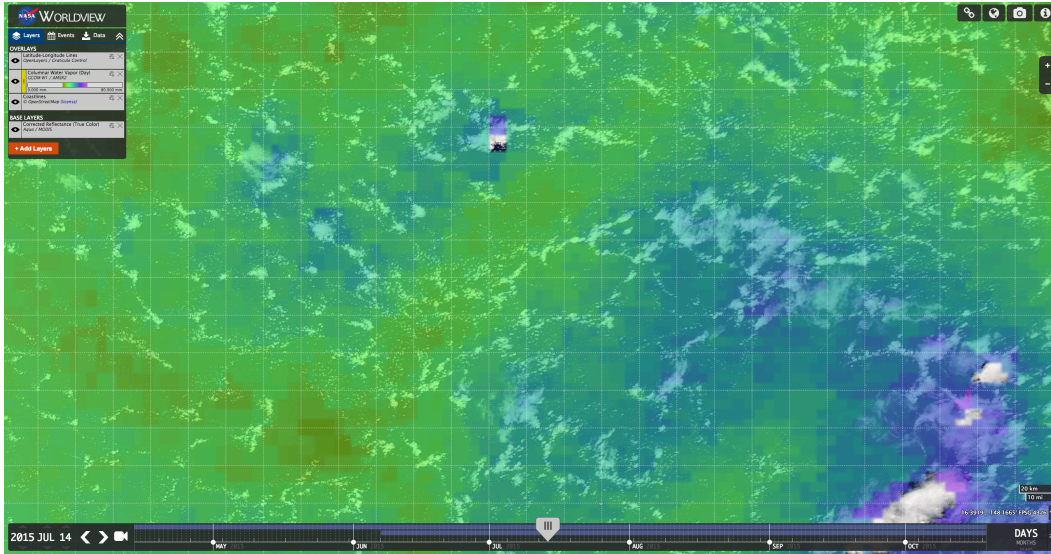


Figure 1. AMSR-2 microwave retrieval of column water vapor path (shading, ranging from 30 kg/m² in brownish-green to 45 kg/m² in purple) overlaid on a visible image from Aqua over a region of aggregated shallow cumulus centered at 17°N, 149°W at about 13:30 local time on July 14, 2015. The overlaid latitude-longitude grid has a spacing of 0.2°. Image is generated from NASA Worldview (<https://worldview.earthdata.nasa.gov>).

Marine boundary-layer cloud regimes worldwide exhibit mesoscale organization, often in the form of the regular patterns of mesoscale cellular convection or MCC [Agee *et al.*, 1973] with a roughly 30:1 aspect ratio of the wavelength to the boundary layer depth [Agee *et al.*, 1973; Wood and Hartmann, 2006]. These include closed cells in shallow stratocumulus layers, and open cells in cumulus and mixed Cu-Sc layers, in both extratropical cold-air outbreaks and subtropical boundary layers. Cumulus clusters like those in Fig. 1a have been interpreted as ‘disorganized’ MCC, which satellite imagery suggests becomes a prevalent form of cloud organization as the marine boundary layer deepens to 2 km or more [Wood and Hartmann, 2006]. Pioneering early observational studies of shallow cumuli over the tropical oceans already noted its propensity to cluster on the mesoscale [Malkus and Riehl, 1964; LeMone and Meitin, 1984].

Numerous theoretical and modeling studies have tried to explain the large aspect ratio of the wavelength of MCC to the boundary layer depth. Early studies interpreted MCC as a form of Rayleigh-Benard convection [Agee *et al.*, 1973]. MCC has a much larger aspect ratio than the 5:1 aspect ratio of dry surface-forced thermal convection [Schroeter *et*

62 *al.*, 2005]; this was rationalized using mechanisms such as anisotropic eddy viscosity or
 63 constant-flux boundary conditions [Agee *et al.*, 1973]. However, these mechanisms don't
 64 explain the multiscale turbulent character of MCC seen in observations and LES; most
 65 of the vertical velocity variance remains in eddy motions of aspect ratios of 3-5 despite
 66 the large aspect ratio of clouds and water vapor [Rothermel and Agee, 1980; Schroeter *et*
 67 *al.*, 2005]. This motivated two new theories of MCC. The first, mesoscale entrainment in-
 68 stability [Fiedler, 1984], only applies to very unusual thermal inversion structures, so it
 69 cannot explain the ubiquity of MCC. The second is that MCC forms from entrainment-
 70 related production of mesoscale humidity variance, e. g. DeRoode *et al.* [2004], which can
 71 occur even in a dry convective boundary layer [Jonker *et al.*, 1999] but is promoted by la-
 72 tent heating and cloud-top radiative cooling [Mueller and Chlond, 1996]. This mechanism
 73 was applied to closed-cell convection and idealizations thereof, for which LES suggests
 74 a gradual increase in aspect ratio as humidity variance grows at large scales. DeRoode
 75 *et al.* [2004] proposed that a humidity variance budget equation could be a useful diag-
 76 nostic for understanding MCC. Kazil *et al.* [2017] suggested that inefficient production of
 77 turbulent kinetic energy at longer wavelengths limits the width of closed cells; however
 78 they focused on the subtle influence of cell scale on the horizontal-mean properties of a
 79 simulated stratocumulus-capped mixed layer rather than on a systematic analysis of how
 80 horizontal humidity variance is generated.

81 LES have shown that precipitation influences MCC. It can force transitions from
 82 closed to open cell MCC by enhancing decoupling and cold pool organization [Wang and
 83 Feingold, 2009], reinforced by aerosol feedbacks, as in pockets of open cells [Berner *et*
 84 *al.*, 2013]. Seifert and Heus [2013] presented LES of mesoscale organization of precipi-
 85 tating shallow cumulus boundary layers. They found that the formation of cold pools by
 86 evaporating precipitation was a prerequisite for aggregation in their simulations, for the
 87 small organizational scales achievable in (25 km)² domains. A follow-on paper by Seifert
 88 *et al.* [2015] found that cold-pool driven mesoscale organization makes this cloud regime
 89 less susceptible to aerosol perturbations.

90 Other methodologies were developed to analyze the self-aggregation of deep cumu-
 91 lus convection first seen in cloud-resolving models [Held *et al.*, 1993; Tompkins, 2001;
 92 Bretherton *et al.*, 2005]. These studies used column-integrated humidity budgets to iso-
 93 late processes that further moisten mesoscale regions that are already moist. They noted
 94 the accuracy of the 'weak temperature gradient' (WTG) approximation that mesoscale

95 horizontal variations in air density (virtual temperature) are negligibly small for unbal-
96 anced circulations smaller than a Rossby radius [*Sobel and Bretherton, 2000; Bretherton et*
97 *al., 2005*]. This approximation has recently been exploited in combination with vertically-
98 resolved humidity and moist static energy budgets in analyses of the Madden-Julian Oscil-
99 lation to associate vertical motions and their effects on the moisture budget with individual
100 physical processes such as convection and radiative heating [*Chikira, 2014; Wolding and*
101 *Maloney, 2015*].

102 We will use an analogous approach to understand mesoscale self-aggregation pro-
103 cesses in LES of shallow cumulus. We frame self-aggregation as an instability of a hori-
104 zontally statistically homogeneous field of cumulus clouds to the spontaneous growth of
105 mesoscale humidity anomalies that span the cumulus layer, pattern the convection and
106 clouds, and create heating perturbations that drive mesoscale circulations. We find that
107 shallow cumulus can aggregate within a day or less due to a fundamentally advective ag-
108 gregation mechanism different from the radiative feedbacks that are critical to deep con-
109 vective self-aggregation [e.g. *Emanuel et al., 2014*], and for which precipitation is not es-
110 sential. This mechanism can be regarded as a form of gross moist instability [*Raymond et*
111 *al., 2009*]. In the simplest case, our mechanism seems related to that proposed for well-
112 mixed stratocumulus by *DeRoode et al. [2004]*, and our use of mesoscale column humidity
113 budgets is analogous to their use of a column-integrated humidity variance budget.

114 Section 2 introduces the LES configuration and key thermodynamic variables used
115 in this analysis. Section 3 discusses the rate of self-aggregation in a control run and sev-
116 eral sensitivity cases. Section 4 analyzes aggregation in the control simulation in terms of
117 a unifying conceptual model based on the WTG approximation. Section 5 derives column
118 mesoscale heat and moisture budgets that elucidate the conditions for self-aggregation,
119 i. e. under which moist regions become moister and dry regions become drier. Section 6
120 considers the mesoscale self-aggregation of shallow cumulus in a minimal-physics setup
121 without precipitation and with horizontally homogeneous radiative heating and surface
122 fluxes. Section 7 presents a discussion and conclusions.

2 Thermodynamic variables and LES model configuration

2.1 SAM LES model

The LES model used in this study is version 6.10 of the System for Atmospheric Modeling (SAM), kindly supplied and maintained by Marat Khairoutdinov and documented by *Khairoutdinov and Randall* [2003] and *Blossey et al.* [2013]. All of our simulations are restricted to warm clouds with liquid condensate only, so the remaining discussion assumes liquid cloud thermodynamics and microphysics. For this case, SAM prognoses four advected scalars, the liquid static energy s_l , the nonprecipitating water mixing ratio $q_n = q_v + q_c$, the rain water mixing ratio q_r , and rain number concentration N_r . The cloud liquid water and temperature are diagnosed from the advected scalars using the assumption of exact grid-scale saturation in cloudy grid cells. Here q_v and q_c are the mixing ratios of water vapor and cloud water, and the liquid static energy is defined

$$s_l = s - L_v(q_c + q_r), \quad (1)$$

where static energy $s = c_p T + gz$, c_p is the isobaric specific heat of dry air, L_v is the latent heat of vaporization, g is gravity, T is temperature and z is height above sea level.

The warm cloud version of the *Morrison et al.* [2005] microphysics scheme is used in these simulations. In this scheme, conversion between cloud and rain water is treated according to *Khairoutdinov and Kogan* [2000]. The cloud droplet size distribution is based on a gamma distribution with a fixed number concentration of $N_d = 100 \text{ cm}^{-3}$ and an exponent $\mu = 10.3$ [*Geoffroy et al.*, 2010]. This cloud droplet size distribution is used to compute cloud droplet sedimentation and the optical properties of cloud liquid [*Neale et al.*, 2012, sec. 4.9.3]. Radiative fluxes are updated every 60 s using the RRTMG scheme [*Mlawer et al.*, 1997], with diurnally-averaged insolation following *Blossey et al.* [2013].

2.2 Domain size and grid resolution

A doubly-periodic domain of horizontal size 128×128 km is used. We choose a relatively coarse grid for computational efficiency, with a horizontal grid spacing of 250 m and a vertical grid spacing that is uniformly 80 m up to 6 km with a stretched grid above, extending to the domain top at 20 km. The computational domain has 512×512×128 grid points in x , y and z , respectively. All simulations are run for 36 hours unless otherwise noted, with an adaptive time step whose average value is 2.5 seconds.

2.3 Control simulation

The control simulation is based on summertime-mean thermodynamic profiles, advective forcings for 17°N, 149°W, the location shown in Fig. 1, which is typified by exactly the mesoscale clusters of Cu rising into surrounding patches of thin Sc that we aim to simulate and understand. It mainly follows the S6 specifications for the CGILS inter-comparison [Blossey *et al.*, 2013] but differs in the following details:

- The duration of the simulation is 72 hours, rather than 10 days.
- Rotational effects are included, using the Coriolis parameter for 17°N. The geostrophic winds are taken equal to the ECMWF winds. The simulated domain-mean wind profile is also nudged to the ECMWF wind profile on a long, twelve hour timescale. The standard CGILS setup nudged the model winds on a ten minute timescale. To minimize oscillations of the winds, the initial wind profiles are the average wind profile over the last six days of a 13.5 day small-domain ($L_x = L_y = 8$ km) simulation.
- The surface fluxes are computed interactively using SAM's surface flux parameterizations and account for local variations in surface wind speed, unlike the idealized surface flux parameterization used in Blossey *et al.* [2013].
- The domain is uniformly translated by the approximate mean wind in the cloud layer ($u = -8.5$ m s⁻¹ and $v = -3$ m s⁻¹), rather than -7 and -2 m s⁻¹, respectively, in Blossey *et al.* [2013]. This minimizes the advection of aggregated patches of cumulus convection across the domain.

2.4 Prognostic equations for s_l and q_t

In our LES, the prognostic equation for s_l is:

$$\frac{Ds_l}{Dt} = S_{s_l} = -\frac{1}{\rho_0} \frac{\partial}{\partial z} (L_v P + F_R) + \left(\frac{\partial \bar{s}_l}{\partial t} \right)_{LS} - w_{LS} \frac{\partial s'_l}{\partial z} + \left(\frac{\partial s_l}{\partial t} \right)_{SGS}, \quad (2)$$

where D/Dt denotes a material derivative, S denotes a source term, $\rho_0(z)$ is the fixed reference density profile, P is the downward precipitation flux relative to the moving air, F_R is the net upward radiative flux, subscript LS refers to large-scale advective forcing (here split into a horizontally uniform component regarded as being applied to the horizontal mean, and vertical advection by w_{LS} of perturbations s'_l from the horizontal mean), and subgrid SGS refers to parameterized subgrid turbulence.

183 A similar prognostic equation is solved in SAM for q_n . However, for budget pur-
 184 poses, it is more elegant to frame the prognostic equation for water substance in terms of
 185 the total water mixing ratio $q_t = q_v + q_c + q_r = q_n + q_r$:

$$186 \quad \frac{Dq_t}{Dt} = S_{q_t} = \frac{1}{\rho_0} \frac{\partial P}{\partial z} + \left(\frac{\partial \bar{q}_t}{\partial t} \right)_{LS} - w_{LS} \frac{\partial q'_t}{\partial z} + \left(\frac{\partial q_t}{\partial t} \right)_{SGS}. \quad (3)$$

187 The mass-weighted vertical integral of q_t , which is the sum of the water vapor path and
 188 the liquid water path (LWP), will be called the total water path (TWP).

189 2.5 Prognostic equation for s_{vl}

190 Horizontal gradients of air density or buoyancy are central to the dynamics of moist
 191 convective boundary layers. We use virtual static energy,

$$192 \quad s_v = c_p T_v + g z, \quad (4)$$

193 as a buoyancy proxy. Here, the virtual temperature $T_v = T(1 + 0.61q_v - q_c - q_r)$ is assumed
 194 to include the loading effect of cloud water and rain water mixing ratio q_r . We stress that
 195 while we must consider virtual effects on air density in our quantitative analysis because
 196 our LES (correctly) includes them, we do not believe that they fundamentally affect the
 197 mechanisms discussed in this paper. That is, if our model neglected these virtual effects, it
 198 would have little impact on the simulated aggregation.

199 For analysis of transport, fluxes, and budgets, it is helpful to work with moist con-
 200 served variables. The linearized virtual liquid static energy,

$$201 \quad s_{vl} = s_l + 0.61c_p T_0 q_t, \quad (5)$$

202 where T_0 is a reference temperature representative of the boundary layer, is a moist-conserved
 203 variable that is an excellent approximation to s_v for unsaturated air, since

$$204 \quad s_v \approx s_{vl} + (L_v - 1.61c_p T_0)(q_c + q_r), \quad (6)$$

205 In this paper, ‘heat’ budgets will actually refer to budgets of s_{vl} . The prognostic
 206 equation for s_{vl} , derived from (3) and (2), is

$$207 \quad \frac{Ds_{vl}}{Dt} = S_{s_{vl}} = -\frac{1}{\rho_0} \frac{\partial}{\partial z} \left((L_v - 0.61c_p T_0)P + F_R \right) + \left(\frac{\partial \bar{s}_{vl}}{\partial t} \right)_{LS} - w_{LS} \frac{\partial s'_{vl}}{\partial z} + \left(\frac{\partial s_{vl}}{\partial t} \right)_{SGS}. \quad (7)$$

3 Mean evolution and aggregation of the control and sensitivity simulations

3.1 Domain-mean evolution

Fig. 2 shows the time-height evolution of the horizontal means of several key variables in the first 36 hours of the control simulation and in two 36-hour simulations in much smaller domains (8 km square) that do not support the development of mesoscale variability. One (S250) is identical to the control run except in domain size; the second (S125) also has a grid spacing half as large (125 m in the horizontal and 40 m in the vertical within the boundary layer).

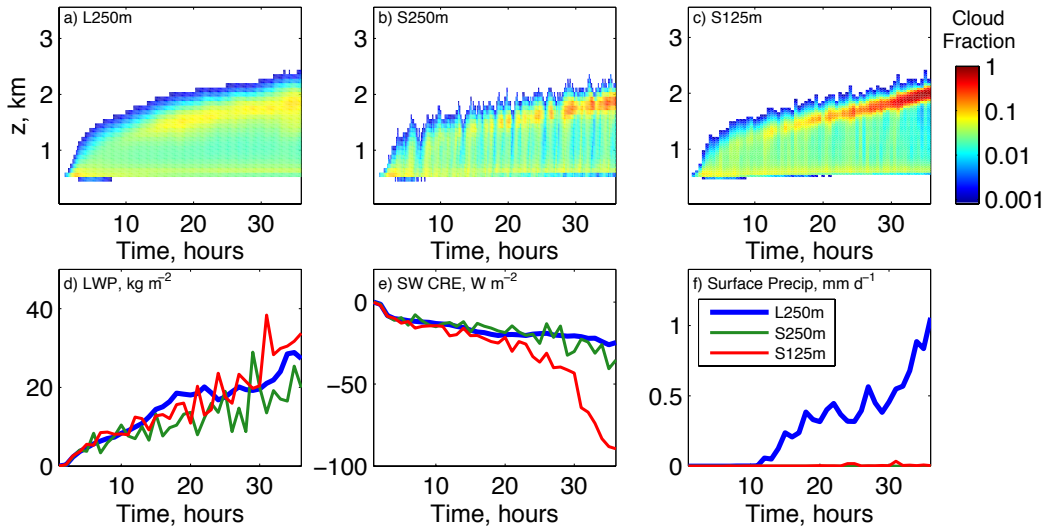


Figure 2. Time-height profiles of horizontally-averaged cloud fraction for (a) the control simulation (L250) with horizontal grid spacing $\Delta x=250$ m), and two other simulations, (b) S250m and (c) S125m, that are identically-configured except for domain size, $L_x=L_y=8$ km, and — in the case of S125m, the horizontal grid spacing $\Delta x=125$ m. At bottom, time series of domain-mean (d) liquid water path, (e) shortwave cloud radiative effect, and (f) surface precipitation.

All of these simulations have a similar horizontal-mean cloud evolution (Fig. 2a-c), with a cumulus-topped boundary layer developing after two hours, deepening rapidly and developing patchy inversion cloud after 6-7 hours and reaching a depth of 2 km by the end of the simulation. The control and S250 simulations also have very similar time series of LWP and shortwave cloud radiative effect (SWCRE). *DeRoode et al.* [2004] and *Xue et al.* [2008] noted a similar insensitivity of horizontal-mean properties of shallow boundary-

227 layer cloud layers to use of a domain size large enough to permit substantial mesoscale
 228 organization.

229 In the control simulation, precipitation sets in after 12 hours and reaches a domain-
 230 mean precipitation rate of over 1 mm/d by 36 hrs. The precipitation is substantially de-
 231 layed in the small domain simulations (as also noted by *Vogel et al.* [2016]); continuations
 232 of these simulations do later generate substantial domain-precipitation rates. Though this
 233 disparity in precipitation has little effect on the cloud properties during our simulations,
 234 that would likely change if the boundary layer deepens further. *Vogel et al.* [2016] found
 235 domain-size sensitivities in domain-mean cloud cover for a precipitating cumulus layer
 236 once some cloud tops in the large-domain simulation exceeded 4 km altitude.

237 Fig. 2 shows that for our case, the domain-mean cloud fraction is more sensitive
 238 to doubling of grid resolution than changes in domain size. Enhanced grid resolution in-
 239 creases the cloud fraction near the inversion, an indicator of reduced penetrative entrain-
 240 ment at stratocumulus and cumulus cloud tops. This substantially increases the SWCRE
 241 toward the end of the simulations.

242 Despite these quantitative sensitivities, our sensitivity experiments don't show a
 243 qualitative change in the cloud and boundary layer structure for a finer grid. A more com-
 244 pelling reason to use a finer grid comes from simulations of deep convective radiative-
 245 convective equilibrium, in which aggregation occurs more readily with a coarser grid
 246 [*Muller and Held, 2012*]. Large-domain simulations with finer grids were too computa-
 247 tionally expensive for this study. Our hope is that an analysis of aggregation in our large-
 248 domain control simulation is at least qualitatively relevant to simulations with similar or
 249 larger domain sizes and finer grid resolutions; that needs to be tested in future.

250 **3.2 Horizontal structure of the aggregating convection**

251 The control simulation strongly aggregates within the first day of evolution. Fig. 3
 252 shows maps of TWP, LWP, and cloud top height at 8-32 hrs. During the first eight hours,
 253 a nearly horizontally homogeneous field of shallow cumulus develops as the underly-
 254 ing boundary layer becomes unstable and starts to convect. By hour 16, there are a few
 255 slightly moister (higher TWP) patches supporting clusters of deeper cumuli, surrounded
 256 by detrained cloud just below the inversion. These continue to amplify rapidly up through
 257 hour 24 and gradually combine into broader patches of moisture and collocated convection

up until 32 hours, when there is one main cluster in the domain. Little further qualitative
change in the aggregation is seen out to the end of the simulation at 72 hours.

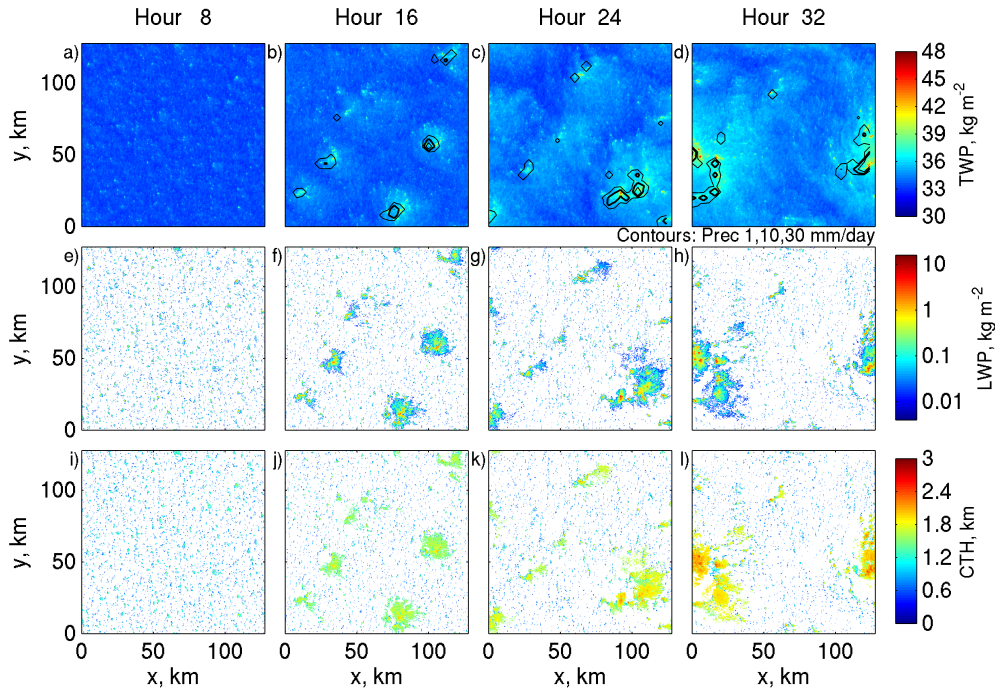
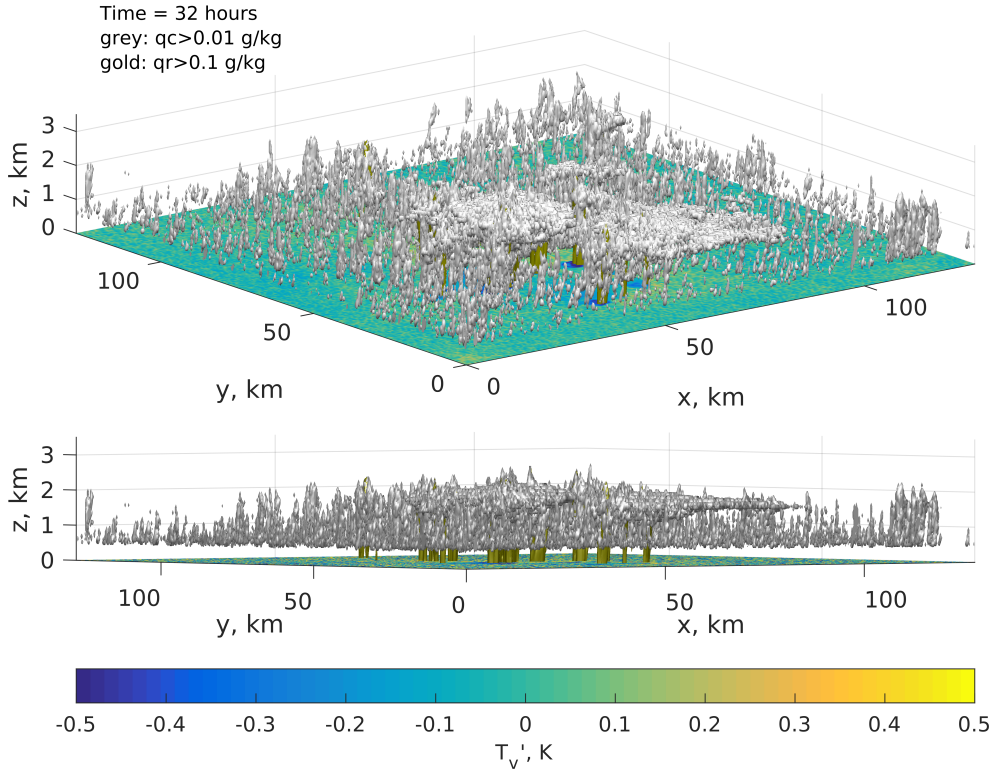


Figure 3. (a-d) Total water path, (e-h) liquid water path and (i-l) cloud-top height in the control simulation
at (a,e,i) 8 hours, (b,f,j) 16 hours, (c,g,k) 24 hours, and (d,h,l) 32 hours.

Fig. 4 shows a perspective plot of the simulated cloud field after 32 hours, periodically translated 48 km in the x direction to avoid visually splitting the main cluster at one of the periodic boundaries of the computational domain. Shallow cumuli surround the single mesoscale cluster of deeper precipitating cumuli and thin inversion cloud.

3.3 Block and quartile description of aggregation

To quantify the evolution of mesoscale variability in the simulated cloud-topped boundary layer, we use means and other statistics over $(16 \text{ km})^2$ horizontal blocks of grid points, averaged over two-hour periods. These mesoscale blocks have been chosen to be large enough to contain an ensemble of clouds sufficient that the block-mean vertical Cu fluxes are a well-defined function of the block-mean thermodynamic profiles (and radia-



266 **Figure 4.** Perspective plot of the cloud field ($q_c > 0.01$ g/kg) and rain ($q_r > 0.1$ g/kg, gold shading) at 32
 267 hours in the control simulation. Sea-surface color shading indicates the virtual temperature anomaly at the
 268 lowest grid level. The displayed domain is periodically translated 48 km from the computational domain to
 269 avoid visually splitting the region of most active convection.

276 tion and surface fluxes, if also needed), but small enough that the simulated aggregation
 277 scale is larger than the block size. From Fig. 3a-d, growing column humidity anomalies
 278 have diameters on the order of 20 km at 16 hr, and broaden at later times; these scales are
 279 efficiently captured with our chosen block size. A similar procedure for analyzing deep
 280 convective self-aggregation was introduced by *Bretherton et al.* [2005]. Other large/small
 281 scale decompositions which additively partition variance could also be used, e.g. Fourier
 282 low/high pass filtering or some form of wavelet decomposition. The block decomposi-
 283 tion has the substantial advantage that all the needed fields and statistics can easily be av-
 284 eraged and saved in-line at each time step within each block, allowing them to be time-
 285 averaged and efficiently stored. We denote perturbations of a mesoscale block average of
 286 some quantity from its domain mean using a subscript m .

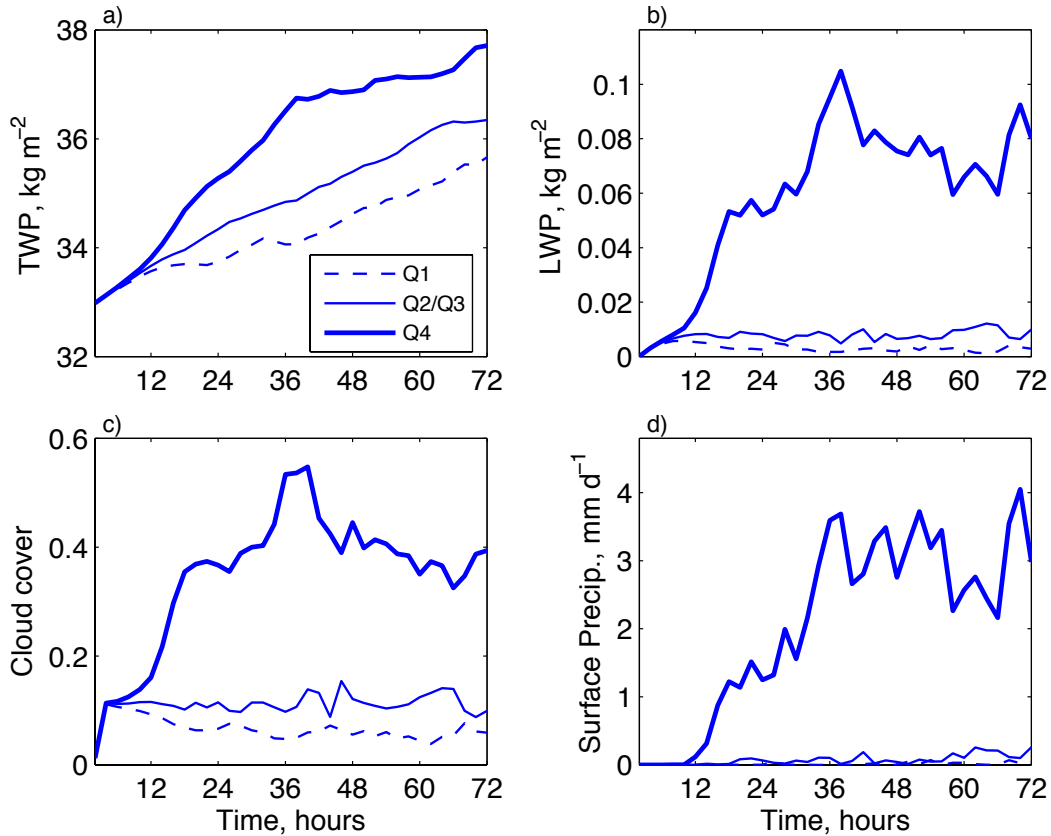
287 Following *Bretherton et al.* [2005], we sort the 64 mesoscale blocks in our com-
 288 putational domain in increasing order of total water path. To summarize the mesoscale
 289 variations that are associated with differences between moist and dry blocks, we com-
 290 pute quartile averages over these blocks, with Q1 being the driest quartile and Q4 being
 291 the moistest quartile. For plotting clarity, we will sometimes lump the two intermediate
 292 quartiles Q2 and Q3 together. The quartile averaging is always with respect to TWP, re-
 293 gardless of the plotted variable. Note that the quartile plots do not show the length scale
 294 of the variability, as long as it is large enough to be resolved by the 16 km block size.

295 Fig. 5 shows such moisture quartile plots for TWP, LWP, cloud cover (the fraction
 296 of columns in the domain containing any cloud), and rainfall. These plots summarize the
 297 aggregation process. At 8 hours, there is very little TWP variability on scales larger than
 298 the width of a single cumulus cloud (Fig. 3a). Fig. 5a shows that the TWP of the moistest
 299 and driest quartiles begin to diverge soon thereafter. Their difference grows nearly expo-
 300 nentially through hour 16, continues to rapidly grow through hour 24, grows more slowly
 301 until hour 36, then levels off and even slightly reduces. This growth of the ‘interquartile’
 302 Q4-Q1 TWP difference is the defining characteristic of mesoscale humidity aggregation.
 303 After aggregation develops, the LWP, cloud cover and rainfall are strongly localized to the
 304 moistest quartile, consistent with the visual impression from Figs. 3c-d.

305 While the humidity and cloud aggregation may be regarded as an instability of a
 306 state of horizontally homogeneous shallow cumulus convection, it quickly deviates from
 307 the expectations of linear instability theory. For an exponentially growing linear instabil-
 308 ity, one would expect the Q4 and Q1 results to diverge exponentially with time, with the
 309 Q2/Q3 average lying half way in between them. In LWP, cloud fraction and precipita-
 310 tion, such behavior is limited to hours 8-11, after which nonlinearities become obvious.
 311 The BOMEX sensitivity study in Section 3.4, in which no extensive cloud patches form at
 312 the inversion, does exhibit a much longer period of slow exponential growth in the TWP
 313 quartile separation, suggesting that inversion cloud patches that form only in the moistest
 314 quartile may be one such source of nonlinearity.

317 **3.4 Sensitivity simulations**

318 We performed several sensitivity simulations, summarized in Table 1 (which also
 319 includes the two small-domain simulations discussed in Section 3.1) to look for factors



315 **Figure 5.** Column humidity quartile-sorted time series of (a) total water path, (b) liquid water path, (c)
 316 cloud cover, and (d) surface precipitation in the control simulation.

320 controlling the existence and rate of aggregation. Fig. 6a-c show quartile plots of TWP
 321 and LWP for these simulations, except Diurnal and FixedInv. All sensitivity simulations
 322 last 36 hours, except BOMEX, which spans 72 hours.

330 Simulations Diurnal and FixedInv test the robustness of features of our case setup.
 331 For brevity, these simulations are described without supporting figures. Simulation Diur-
 332 nal includes a diurnal cycle of insolation corresponding to the S6 location, assuming the
 333 simulation is initialized at 0 UTC, which is the late afternoon in local time. It aggregates
 334 quite similarly (in terms of Q4-Q1 TWP spread) to CTL, as does a similar simulation ini-
 335 tialized at 12 UTC.

336 In FixedInv, the subsidence rate is adaptively adjusted to maintain a constant inver-
 337 sion height of 1800 m using the method of *Blossey et al.* [2009]. Again, the aggregation
 338 develops similarly to the control simulation, as measured by Q4-Q1 TWP spread, though

Table 1. List of Sensitivity Simulations

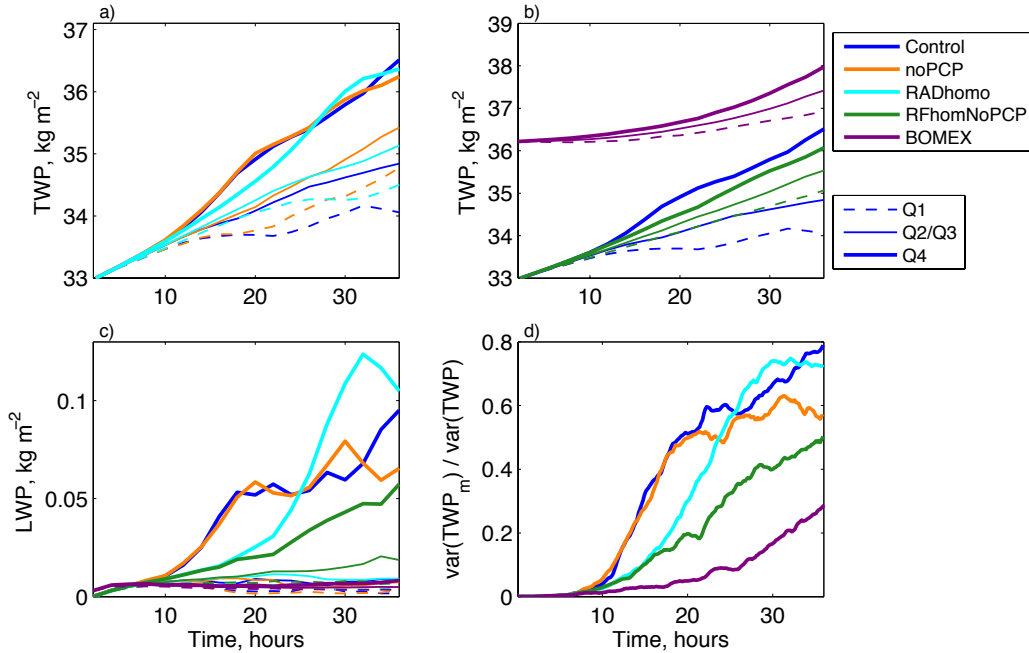
Name	Description
Control	Based on present-day S6 case in <i>Blossey et al.</i> [2013], 128×128 km domain, $\Delta x = 250$ m, $\Delta z = 80$ m
S250	As in control, except with a small horizontal domain of 8×8 km
S125	As in S250, except using halved grid spacings $\Delta x = 125$ m, $\Delta z = 40$ m
Diurnal	As in control, but with diurnal cycle of insolation
FixedInv	As in control, but with mean subsidence increased to keep inversion height fixed
noPCP	As in control, except that rain formation and sedimentation are prohibited
RADhomo	As in control, except that radiative heating rates are horizontally homogenized
RFhomNoPCP	As in noPCP, except that both surface fluxes and radiative heating rates are horizontally-homogenized
BOMEX	Based on BOMEX case in <i>Siebesma et al.</i> [2003], with same domain and grid as control

339 the domain-mean TWP now stays nearly constant throughout the simulation. In FixedInv,
 340 the size of the moist patches does not grow as fast as in CTL, and stays smaller than the
 341 domain size throughout the simulation.

342 The remaining simulations test the sensitivity of the aggregation to changes in the
 343 physics included in the model, as well as the thermodynamic profiles assumed. Simulation
 344 noPCP is similar to the control (CTL), except that precipitation is suppressed. Figs. 6a,c
 345 show that this has a minimal impact on the initial humidity and LWP aggregation, though
 346 it slightly reduces the aggregation at later times.

347 Simulation RADhomo is similar to CTL, except that the computed radiative heating
 348 rate is horizontally homogenized to prevent any local feedback on the growth of mesoscale
 349 cloud and humidity anomalies. Figs. 6a,c show that the moisture and LWP begin to ag-
 350 gregate more slowly but later appear to catch up with, or in the case of LWP, exceed the
 351 aggregation evinced by CTL.

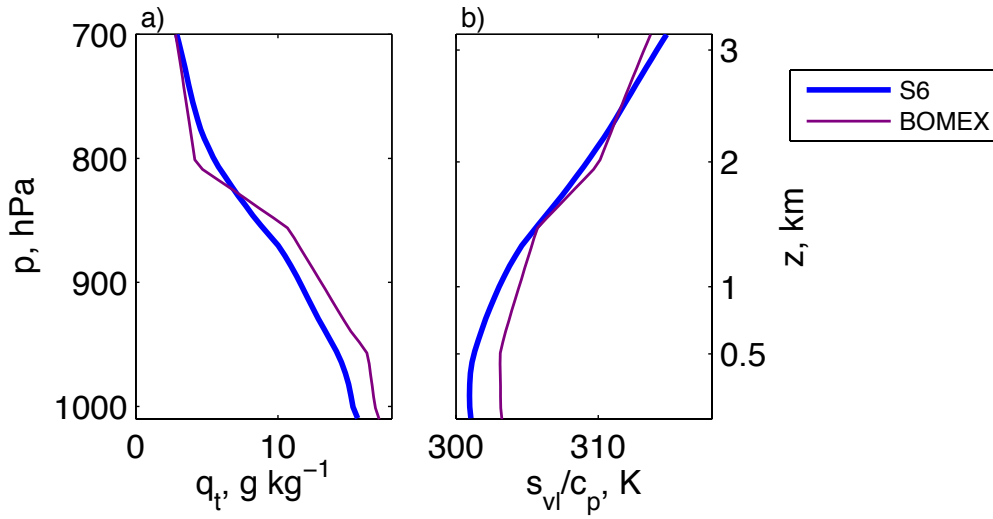
352 In simulation RFhomNoPCP, both the radiative and surface fluxes are horizontally
 353 homogenized, and precipitation is suppressed. Our last sensitivity study uses a different
 354 initial thermodynamic profile and specified horizontally homogeneous advective/radiative
 355 and surface flux forcings from the GEWEX Cloud System Study Barbados Oceanographic
 356 and Meteorological Experiment (BOMEX) intercomparison [*Siebesma et al.*, 2003]. This



324 **Figure 6.** Top: Comparison of column humidity quartile-sorted time series of total water path for (a)
 325 control, no-precipitation (noPCP) and horizontally-homogenized radiation (RADhomo) simulations and (b)
 326 control, nonprecipitating horizontally-homogenized radiation and surface flux (RfhomNoPCP) and BOMEX
 327 simulations. Bottom: Comparisons for all sensitivity simulations of (c) column humidity quartile-sorted time
 328 series of liquid water path and (d) the ratio of the variance of the block-averaged total water path to that of the
 329 unfiltered total water path.

357 simulation is also specified to be nonprecipitating. It is like RfhomNoPCP except that the
 358 initial temperature profile is less strongly stratified and the free troposphere is drier, as
 359 shown in Fig. 7. Fixed forcing profiles for temperature and humidity tendency represent
 360 the combined effects of horizontal advection and radiative cooling.

363 Fig. 6b compares moisture quartile time series from RfhomNoPCP and BOMEX
 364 with the control case. Both systematically aggregate column humidity, albeit more slowly
 365 than in CTL. We have continued the BOMEX simulation out to 72 hours to confirm that
 366 the aggregation continues to develop. In the RfhomNoPCP case, inversion cloud patches
 367 that enhance LWP develop in the moistest quartile (Fig. 6c). The BOMEX case does not
 368 sustain a large enough relative humidity at the inversion base to support inversion cloud.
 369 We speculate that this is due to its drier free troposphere and weaker lower tropospheric
 370 stability. As a result, BOMEX develops little LWP even in the moistest quartile, though



361 **Figure 7.** Initial profiles of (a) total water mixing ratio q_t and (b) virtual liquid static energy s_{vl}/c_p (a
 362 buoyancy surrogate outside cloud scaled into temperature units) for S6 and BOMEX.

371 still more than in the drier quartiles. In the BOMEX case, an approximately exponential
 372 growth of Q4-Q1 TWP difference with an e -folding timescale of about 15 hours occurs
 373 throughout the simulation.

374 An alternate nondimensional metric of mesoscale aggregation can be formed by first
 375 calculating for each block its block-average (‘mesoscale’) total water path anomaly TWP_m
 376 from the domain-mean. The ratio of the spatial variance of TWP_m to that of the raw
 377 TWP can be interpreted as the mesoscale fraction of the TWP variance. Fig. 6d shows
 378 time series of this ratio for the simulations discussed thus far. It confirms that during the
 379 spread of Q4-Q1 TWP difference after hour 10 seen in Figs. 6a-b, mesoscale variability
 380 starts to dominate the overall TWP variance between grid columns, indicating a state of
 381 mesoscale column humidity aggregation.

382 The TWP variance ratio metric can easily be quantitatively compared across cases
 383 and cloud regimes. Its dependence on the choice of block size should be weak for block
 384 sizes intermediate between the cumulus scale and the dominant aggregation scales. Alter-
 385 nate versions of the metric could be defined using other (possibly observationally-derived)
 386 quantities, such as outgoing longwave radiation, as a complement to the cluster-based
 387 analysis of *Tobin et al.* [2012].

388 These sensitivity simulations suggest that neither precipitation nor mesoscale feed-
 389 backs of radiation or surface fluxes are essential for aggregation of a shallow cumulus
 390 boundary layer. However, local cloud-radiation feedback does speed up the initial mois-
 391 ture aggregation, and precipitation enhances aggregation toward the end of the simulation,
 392 as the boundary layer deepens and rains more.

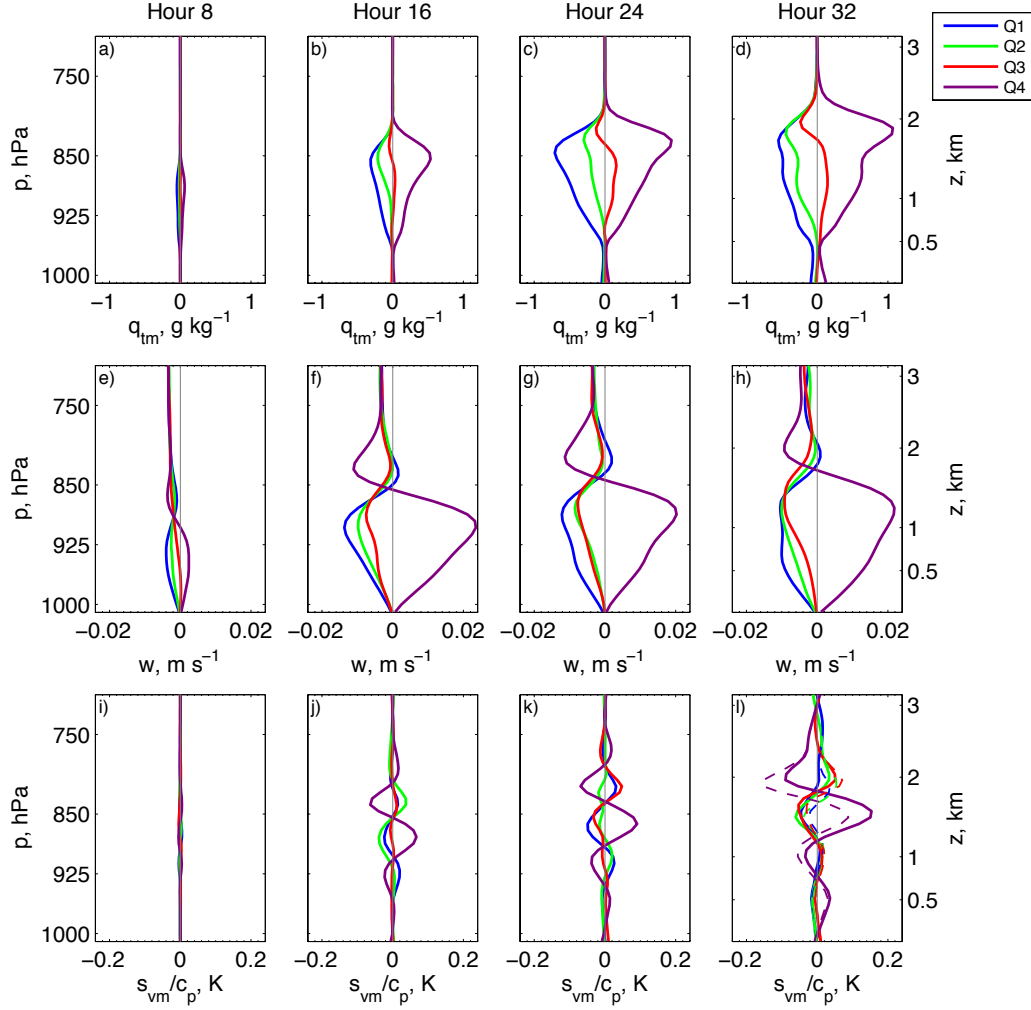
393 **4 Analysis of aggregation of the control simulation**

394 **4.1 Moisture and liquid water profiles**

395 Figs. 8a-d show moisture quartile-sorted profiles of the mesoscale block-averaged
 396 humidity anomaly q_{tm} from the domain mean, averaged over two hour blocks ending at
 397 8, 16, 24 and 32 hours. In the moistest quartile (Q4), the entire cumulus layer, from cloud
 398 base at 500 m to the highest cloud tops, is moistened, most strongly at the inversion base.
 399 By 24 hours, the humidity anomaly at the inversion base reaches 1 g/kg, or about 10%
 400 in relative humidity, after which it grows much more slowly. Even as early as 16 hours,
 401 the Q4 moisture anomalies are stronger and have a more top-heavy vertical profile than
 402 the dry quartile (Q1) anomalies. Remarkably, there are almost no mesoscale humidity per-
 403 turbations in the subcloud layer, below 500 m altitude. This is because the sea surface
 404 temperature and the initial humidity field are horizontally homogeneous, and precipitation
 405 is too weak to drive vigorous cold pools that couple the subcloud layer temperature and
 406 humidity to the cumulus convection.

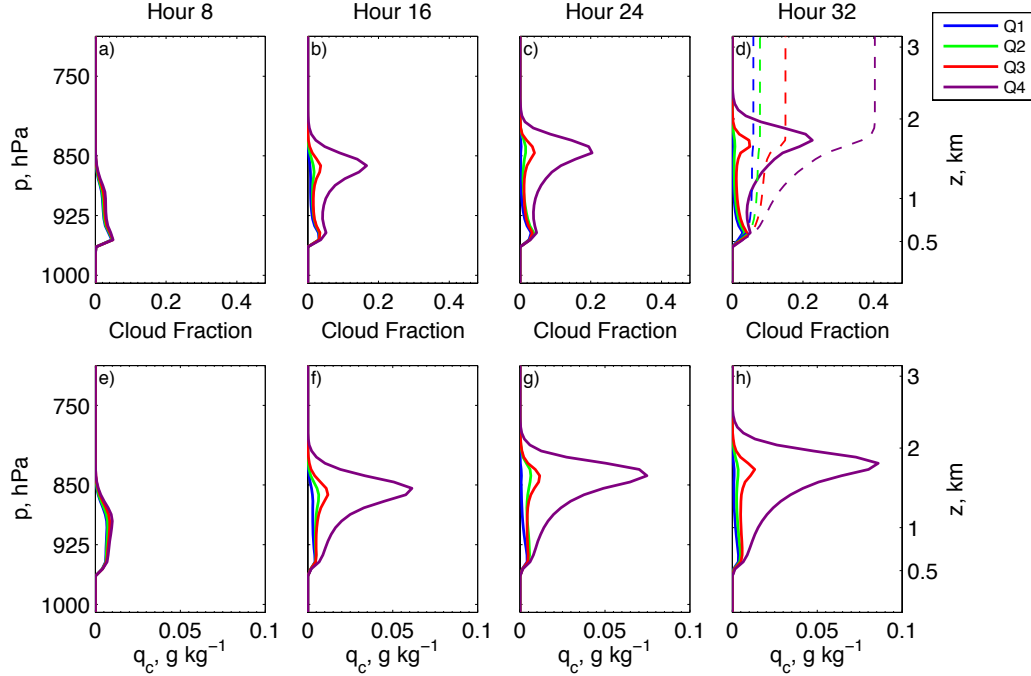
411 Fig. 9 shows corresponding profiles of cloud fraction and cloud liquid water content
 412 q_c . They also show little interquartile separation near the cumulus base, but there is much
 413 more cloud in the moistest quartile throughout the rest of the cumulus layer and especially
 414 just below the inversion base. Remote sensing observations of Barbados trade cumuli by
 415 *Nuijens et al.* [2014] also show that cloud fraction is much more variable near the inver-
 416 sion than at the base of the cumulus layer on time scales of hours or longer.

420 Tropical shallow cumulus boundary layers do often show mesoscale moisture per-
 421 turbations in the subcloud layer, which are correlated with overlying patches of shallow
 422 cumulus convection in observations [*LeMone and Meitin*, 1984] and in LES [*Seifert and*
 423 *Heus*, 2013]. This patchiness may be a remnant of cold pools generated from prior pre-
 424 cipitating convection, which take many hours to be damped out by surface flux feedbacks
 425 [*Johnson and Nicholls*, 1983]. Subsynoptic humidity variability due to large-scale dynam-



407 **Figure 8.** Column humidity quartile-sorted profiles of mesoscale anomalies (a-d) q_{tm} , (e-h) $w = \bar{w} + w_m$,
 408 and (i-l) s_{vm}/c_p averaged over two-hour periods ending at (a,e,i) 8 hours, (b,f,j) 16 hours, (c,g,k) 24 hours
 409 and (d,h,l) 32 hours into the control simulation. For the final period, the mesoscale anomalies of virtual liquid
 410 static energy s_{vlm}/c_p are plotted as dashed lines along with those of s_{vm}/c_p in panel (l).

426 ics or mesoscale SST anomalies could also drive mesoscale humidity perturbations. Were
 427 such pre-existing perturbations added to the initial humidity distribution, they would likely
 428 modulate the early development of cumulus clouds and couple to the humidity-convection
 429 aggregation.



417 **Figure 9.** As in figure 8, except for (a-d) cloud fraction and (e-h) cloud water. Quartile-sorted profiles of
 418 cumulative cloud fraction (computed upwards) are plotted as dashed lines along with cloud fraction in panel
 419 (d).

4.2 WTG approximation

430
 431 The bulk of a shallow cumulus boundary layer is stably stratified. Within and below
 432 active cumuli, condensation and evaporation can generate small-scale heating and buoy-
 433 ancy anomalies. Gravity waves constantly spread out these horizontal density perturba-
 434 tions and inhibit them from building up on the mesoscale [Bretherton and Smolarkiewicz,
 435 1989].

436 Figs. 8i-l show quartile-sorted vertical profiles of mesoscale (block-mean) perturba-
 437 tions of s_v/c_p , a proxy for buoyancy, averaged over two-hour periods ending at 8, 16, 24
 438 and 32 hours. As the mesoscale aggregation develops, these perturbations grow and satu-
 439 rate, but they remain quite small – less than 0.2 K. Thus our simulations accurately obey
 440 the weak temperature gradient approximation (WTG) that mesoscale (block-mean) buoy-
 441 ancy perturbations remain negligibly small,

442
$$s_{vm} \approx 0, \tag{8}$$

443 despite significant sources of mesoscale heating and cooling due to the collective action
 444 of precipitation, radiation, turbulence and shallow cumulus convection. Those localized
 445 heat sources instead induce mesoscale vertical motions whose associated adiabatic cooling
 446 compensates the localized heating. Like our simulations, aircraft observations of MCC
 447 are consistent with WTG. They do not show substantial mesoscale virtual temperature
 448 perturbations collocated with more humid regions and thicker clouds [*Agee and Lomax,*
 449 1978].

450 We use a slightly modified formulation of WTG based on the observation that the
 451 mesoscale-averaged liquid water content is small at all levels in a shallow cumulus cloud
 452 field. Thus, the smallness of mesoscale-averaged variations of s_v also carries over to mesoscale-
 453 averaged variations of the virtual liquid static energy $s_{vl} = s_v - L_{vl}(q_c + q_r)$ introduced
 454 in Eqs. (5) and (6), which is a moist-conserved variable more suitable for budget analy-
 455 ses. The quartile-sorted profiles of s_{vl}/c_p averaged over the two-hour period ending at 32
 456 hours, are shown as dashed lines in Fig. 8l. They are recognizably similar to the corre-
 457 sponding profiles of s_v/c_p (solid lines in the same panel) and equally small; similar re-
 458 sults hold for other times. Hence we can regard s_{vlm} as a reasonable mesoscale buoyancy
 459 proxy in our simulations, and our modified version of WTG is phrased

$$460 \quad s_{vlm} \approx 0. \quad (9)$$

461 **4.3 Mesoscale vertical motions**

462 Figs. 8e-h show the moisture quartile-sorted profiles of vertical motion w at the four
 463 selected times. For each altitude in each block, the mean w is the sum of the prescribed
 464 domain-mean \bar{w} and the simulated block-mean mesoscale anomaly w_m . Near the top of
 465 the cumulus layer, the latter grows to 2 cm/s averaged over the moist quartile of blocks,
 466 dominating the domain-mean subsidence. At all times, the mesoscale vertical motions
 467 have a dipole structure, with ascent in moist regions through most of the boundary layer
 468 in the moistest quartile, but descent in the inversion layer. According to WTG, these ver-
 469 tical motions are driven by anomalous heating of the lower part of the boundary layer and
 470 cooling of the inversion layer in moister columns, induced by small-scale turbulence and
 471 convective processes and their effects on latent, radiative and surface-driven heating. Like
 472 the profiles of liquid water, the w_m profiles quickly become asymmetric between moist
 473 and dry regions.

4.4 Conceptual model of aggregating shallow cumulus

Fig. 10 presents a schematic of the aggregating boundary layer based on the results so far. This schematic will be useful for visualizing the mesoscale heat and moisture budgets, quantified in Sections 5.1 and 5.2, respectively.

The blue dashed lines show the base and top of the inversion layer. They are flat because virtual temperature is approximately horizontally homogeneous (WTG). In the moist patch at the center of the diagram, cumulus updrafts lose less buoyancy to entrainment-induced evaporative cooling, so they deepen into the inversion layer and may detrain horizontally extensive patches of inversion cloud at its base. Air rising through the lower parts of these cumulus clouds condenses liquid water and releases latent heat within the mesoscale moist patch, inducing mesoscale upward motion (realized as increased updraft mass flux within the cumuli) within the moist patch. These cumuli also penetratively entrain drier air from within the inversion layer, evaporating and cooling their tops and inducing mesoscale subsidence there.

Associated with these vertical motions, there must be horizontal convergence into the moist patch throughout the lower part of the boundary layer and near the inversion top, and divergence at the inversion base. The associated net column-integrated moisture convergence helps determine whether moist patches tend to further moisten, promoting self-aggregation.

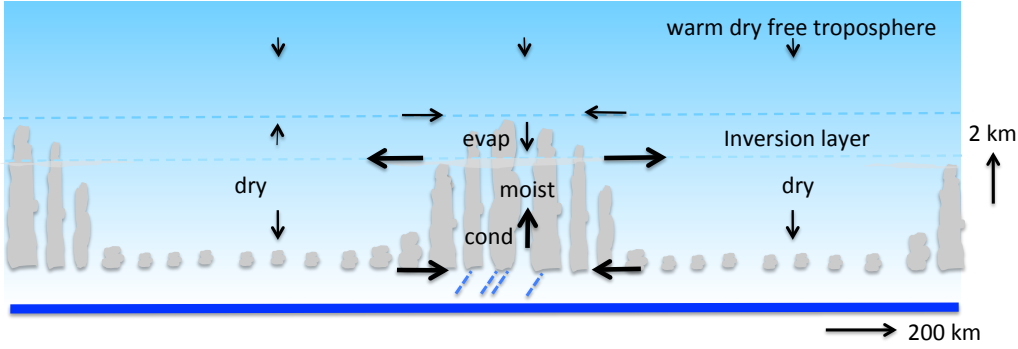
4.5 Mesoscale cumulus heating and moistening

A key ingredient in our schematic is how vertical transports of heat and moisture by shallow cumulus and turbulence depend on the humidity of a mesoscale patch. Here we diagnose this dependence in the LES.

Each variable $f(\mathbf{x}, t)$ is described in terms of its domain mean \bar{f} , and its deviation f' from that mean. In each block, that deviation is partitioned into the block-horizontal-mean deviation f_m and a ‘cumulus-scale’ deviation f_c , which is the local difference of f from its block mean:

$$f(\mathbf{x}, t) = \bar{f}(t) + f'(\mathbf{x}, t), \quad f' = f_m(\mathbf{x}, t) + f_c(\mathbf{x}, t). \quad (10)$$

With this definition, the mesoscale deviation is horizontally uniform across each block, and its horizontal average over all blocks is zero. The cumulus-scale deviation has a zero



493 **Figure 10.** Schematic of processes accompanying shallow convective aggregation. On mesoscales, the
 494 virtual temperature remains flat on mesoscales but moist and dry patches develop. The moist patches support
 495 deeper and more vigorous cumulus convection, driving condensational heating and mesoscale ascent in the
 496 conditionally unstable layer and penetrative entrainment-induced evaporative cooling and mesoscale subsi-
 497 dence in the overlying inversion layer. The moist patches become moister via low-level humidity convergence
 498 but dry from penetrative entrainment and precipitation.

510 horizontal average across each block but captures the horizontal variability within that
 511 block.

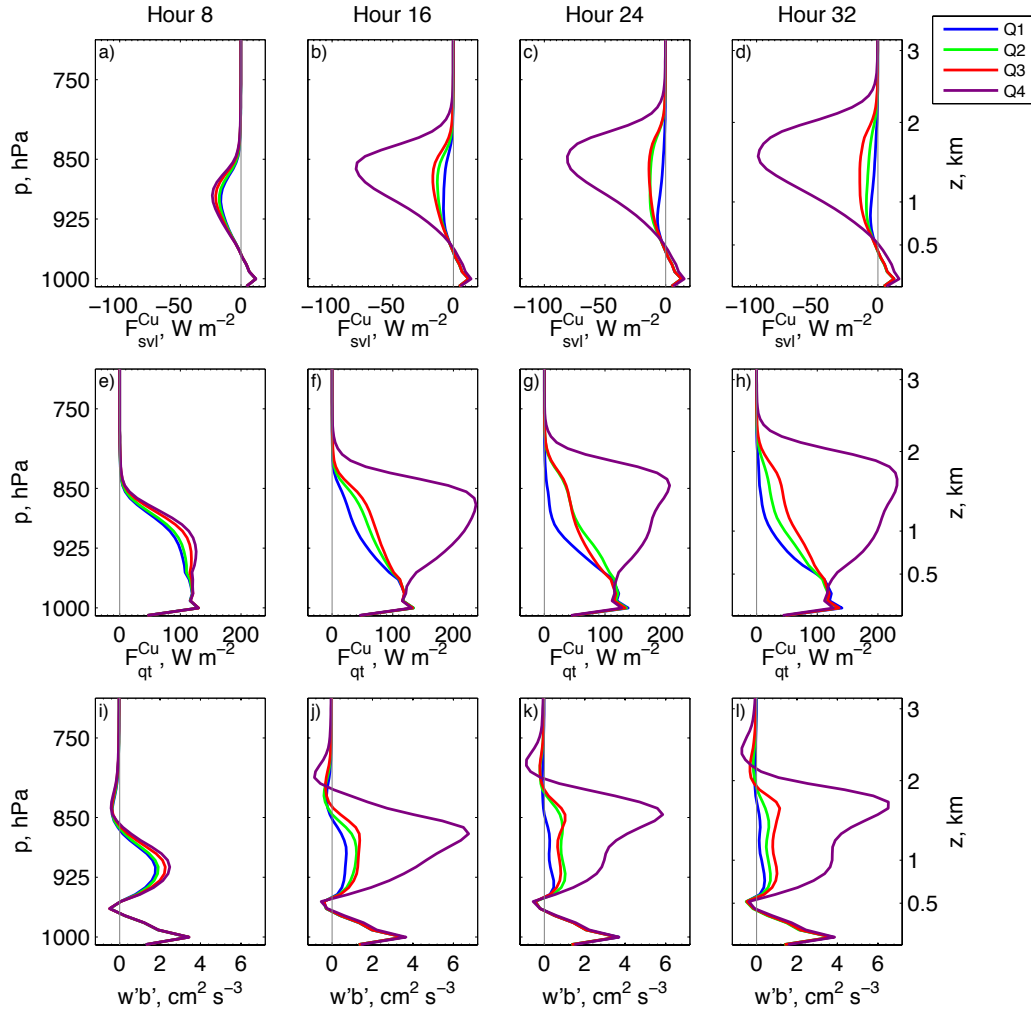
512 We also define the cumulus-scale covariance between two variables f and g within
 513 each block to be $[f_c g_c]$, where the square brackets indicate a horizontal average over a
 514 block. We define the block-mean vertical ‘cumulus’ fluxes of f (which also include effects
 515 of other resolved-scale turbulence) as

$$516 \quad F_f^{Cu} = \rho_0 [w_c f_c]. \quad (11)$$

517 Each block has a different profile of the cumulus flux of f . The domain-mean vertical
 518 flux of f is $\rho_0(\overline{w_m f_m} + [w_c f_c])$, a sum of mesoscale and Cu-scale contributions.

519 Fig. 11(a-h) shows moisture quartile-sorted profiles of the cumulus s_{vl} and q_t fluxes,
 520 which are strongest near the inversion base. The cumulus updrafts have anomalously high
 521 q_t (upward q_t flux) but low s_{vl} (downward s_{vl} flux). Below the cumulus base near 0.6 km
 522 altitude, there is no difference between the heat and moisture fluxes between the moist
 523 and dry quartiles. At hour 8 the fluxes within the cumulus layer are only slightly different
 524 between quartiles, but at later times, the fluxes are strongly concentrated in the moistest

525 quartile, where they are also more ‘top-heavy’, reflecting the deeper cumulus convection
 526 there. The fluxes in the moistest quartile reach maximum strength quickly, after 16 hours.



527 **Figure 11.** As in figure 8, except for (a-d) cumulus s_{vl} flux, (e-h) cumulus q_t flux, and (i-l) buoyancy flux.

528 According to the conceptual model, cumulus updrafts should better maintain their
 529 buoyancy as their rise in moister regions. Thus, we expect the buoyancy flux to be larger
 530 in moist regions. Fig. 11(i-l) shows that this is indeed the case. At 16 hours and later, in
 531 the moistest quartile the buoyancy flux throughout the cumulus layer is upward throughout
 532 the cumulus layer, except in the upper reaches of the inversion, while in the other quartiles
 533 the buoyancy flux is highly suppressed more than 100 m above the cumulus base.

5 Perturbation and mesoscale budget equations for heat and moisture

The prognostic equation for horizontal perturbations of a general prognosed scalar f with source S_f is

$$\frac{\partial f'}{\partial t} = -\mathbf{u}_h \cdot \nabla_h f' - w \frac{\partial f'}{\partial z} - w' \frac{d\bar{f}}{dz} + S_f'. \quad (12)$$

Note that unprimed quantities still include their horizontal domain-mean. We will later partition this equation into mesoscale and Cu-scale components as needed.

Our LES uses the anelastic equations with a reference density profile $\rho_0(z)$. We will make use of the anelastic mass conservation equation

$$\nabla_h \cdot \mathbf{u}_h + \rho_0^{-1} \frac{\partial}{\partial z} (\rho_0 w) = 0. \quad (13)$$

5.1 The mesoscale s_{vl} budget including WTG simplifications

For each block, we form a prognostic equation for the block averaged perturbation s_{vlm} , which we simplify using WTG. This involves block-averaging the perturbation equation (12) for s_{vl} and neglecting the tendency term on the LHS using the WTG approximation (9) that $s_{vlm} \approx 0$:

$$0 \approx \frac{\partial s_{vlm}}{\partial t} = - \left[\mathbf{u}_h \cdot \nabla_h s'_{vl} + w \frac{\partial s'_{vl}}{\partial z} \right]_m - w_m \frac{d\overline{s_{vl}}}{dz} + S_{svlm}. \quad (14)$$

WTG also implies that $s'_{vl} = s_{vlm} + s_{vlc} \approx s_{vlc}$. Using this together with the anelastic mass conservation equation (13), we can express the advection of s'_{vl} by the full velocity field as

$$\begin{aligned} \left[\mathbf{u}_h \cdot \nabla_h s'_{vl} + w \frac{\partial s'_{vl}}{\partial z} \right]_m &= \frac{1}{\rho_0} \left[\nabla \cdot (\rho_0 \mathbf{u} s'_{vl}) \right]_m \\ &= \frac{1}{\rho_0} \left[\nabla \cdot (\rho_0 (\bar{\mathbf{u}} + \mathbf{u}_m + \mathbf{u}_c) s_{vlc}) \right]_m \\ &= \frac{1}{\rho_0} \left[\nabla \cdot (\rho_0 \mathbf{u}_c s_{vlc}) \right]_m \\ &= \left[\nabla_h \cdot (\mathbf{u}_{hc} s_{vlc}) \right]_m + \frac{1}{\rho_0} \frac{\partial}{\partial z} \left[\rho_0 w_c s_{vlc} \right]_m \\ &\approx \frac{1}{\rho_0} \frac{\partial}{\partial z} \left[\rho_0 w_c s_{vlc} \right]_m. \end{aligned} \quad (15)$$

In the final step, we justify neglecting the horizontal divergence term by applying the divergence theorem around the block, invoking scale separation between the mesoscale block size L_B and the boundary-layer depth H , which we assume also scales the Cu-scale

560 motions, and applying a scaling argument:

$$\begin{aligned}
 561 \quad [\nabla_h \cdot (\mathbf{u}_{hc} s_{vlc})]_m &= L_B^{-2} \int_{\partial B} (\mathbf{u}_{hc} \cdot \mathbf{n}) s_{vlc} dl \\
 562 &\sim L_B^{-2} \cdot 4L_B \cdot U \cdot S \sim US/L_B.
 \end{aligned} \tag{16}$$

563 Here ∂B is the horizontal block edge, U is a convective velocity scale, and S is a scale for
 564 convective s_{vl} perturbations. If we assume that w_c also scales with U , the corresponding
 565 vertical derivative term scales as

$$566 \quad \frac{1}{\rho_0} \frac{\partial}{\partial z} [\rho_0 w_c s_{vlc}]_m \sim US/H. \tag{17}$$

567 Thus, the horizontal divergence can be neglected compared to the vertical derivative since
 568 the block size $L_B \gg H$.

569 Finally, the source term S_{svl} was given in the corresponding s_{vl} advection equation
 570 (7). Neglecting the very small contribution of subgrid turbulent mixing, and noting that
 571 the large-scale forcing is horizontally homogeneous, the block-mean variations of S_{svl} are
 572 due to latent heating and radiative flux convergence:

$$573 \quad S_{svlm} = -\frac{1}{\rho_0} \frac{\partial}{\partial z} \left((L_v - 0.61c_p T_0) P + F_R \right)_m. \tag{18}$$

574 Following *Bretherton and Wyant* [1997], it is convenient to define the nondimen-
 575 sional thermodynamic parameter

$$576 \quad \mu = 1 - 0.61c_p T_0 / L_v \approx 0.93. \tag{19}$$

577 We substitute Eqns. (15), (18), and (19) into (14):

$$578 \quad 0 \approx -\frac{1}{\rho_0} \frac{\partial}{\partial z} F_{svlm}^{Cu} - w_m \frac{d\bar{s}_{vl}}{dz} - \frac{1}{\rho_0} \frac{\partial}{\partial z} (\mu L_v P + F_R)_m. \tag{20}$$

579 This equation includes sources due to cumulus flux convergence and mesoscale verti-
 580 cal advection as well as the diabatic sources of s_{vl} from latent heating and radiation. In
 581 the spirit of WTG, we solve it for the block-average vertical velocity w_m in terms of the
 582 block-averaged source terms, which sum to the apparent heating S_{svlm}^{app} . In addition to the
 583 diabatic heating rates in (18) from precipitation and radiation, the apparent heating also
 584 includes a contribution from the cumulus flux convergence of s_{vl} :

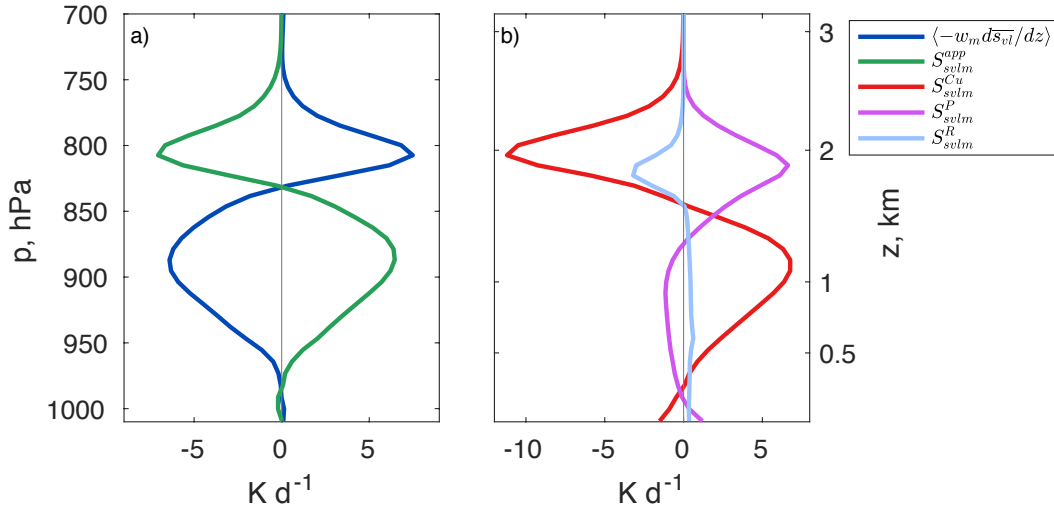
$$585 \quad w_m \frac{d\bar{s}_{vl}}{dz} \approx S_{svlm}^{app} = S_{svlm}^{Cu} + S_{svlm}^P + S_{svlm}^R, \tag{21}$$

586 where

$$587 \quad (S_{svlm}^{Cu}, S_{svlm}^P, S_{svlm}^R) = -\frac{1}{\rho_0} \frac{\partial}{\partial z} (F_{svl}^{Cu}, \mu L_v P, F_R)_m. \tag{22}$$

588 This decomposition is analogous to similar WTG analyses for deep convection that ne-
 589 glected virtual effects [Chikira, 2014; Wolding and Maloney, 2015].

590 We test how well this applies to our control simulation averaged over a representa-
 591 tive 8-hour time interval, 24–32 hours, using averages over the moistest quartile of sub-
 592 domains. WTG applies more accurately for an 8-hour average than for the two-hour av-
 593 eraging period used for earlier profile plots, because it takes time to spread mesoscale s_v
 594 anomalies across the domain. On the other hand, 8 hours is still short enough to analyze
 595 the relatively slow evolution of moisture self-aggregation. Fig. 12a shows that there is a
 596 close balance between the profiles of the mesoscale advective heating $-w_m d\bar{s}_v/dz$ and
 597 the mesoscale apparent heating anomaly S_{svlm}^{app} , as predicted by (21) based on the WTG
 598 approximation. The vertical dipole structure of S_{svlm}^{app} shows the expected structure of ap-
 599 parent heating in the bulk of the cumulus layer below apparent cooling in the inversion
 600 layer.



601 **Figure 12.** Profiles of moist quartile anomalies averaged over 24–32 hrs from the control simulation of: (a)
 602 Mesoscale advective warming $-w_m d\bar{s}_v/dz$ and apparent heating S_{svlm}^{app} ; (b) Contributions to the apparent
 603 heating profile from cumulus convection, precipitation and radiation.

604 Fig. 12b shows the partitioning of the apparent heating anomaly into cumulus, pre-
 605 cipitation and radiation contributions based on (22). The contribution from the cumulus
 606 flux is dominant, but the contribution from precipitation is also significant by this time,
 607 compensating for more than half of the cumulus-flux cooling within the inversion layer,
 608 in which the deepest cumuli reach. Between 0.1-1.4 km elevation (the subcloud layer and

609 the lower part of the cumulus layer), there is slight cooling due to net evaporation of pre-
 610 cipitation. Radiation also contributes to apparent anomalous cooling in the inversion layer,
 611 where the moist quartile has substantially more cloud.

612 An important difference between the three terms is their vertically-integrated contri-
 613 bution to the apparent heating. Denote a mass-weighted column integral of any quantity f
 614 from the surface to the domain top using angle brackets:

$$615 \quad \langle f \rangle = \int_0^\infty \rho_0 f dz. \quad (23)$$

616 Since the cumulus s_{vl} flux vanishes above the inversion, the column integral of its mesoscale
 617 anomaly is

$$618 \quad \langle S_{svlm}^{Cu} \rangle = -\left\langle \frac{1}{\rho_0} \frac{\partial}{\partial z} F_{svlm}^{Cu} \right\rangle_m = F_{svlm}^{Cu}(z=0), \quad (24)$$

619 which is the mesoscale anomaly of the surface s_{vl} flux. Similarly,

$$620 \quad \langle S_{svlm}^P \rangle = \mu L_v P_m(z=0) \quad (25)$$

$$621 \quad \langle S_{svlm}^R \rangle = -\Delta F_{Rm}, \quad (26)$$

622 where $P_m(z=0)$ is the surface precipitation rate anomaly, and ΔF_{Rm} is the mesoscale
 623 anomaly in the column-integrated radiative flux divergence. In the control run, there is
 624 more precipitation but also more radiative cooling in moist regions, while the surface
 625 flux anomalies are small. Thus, the column-integrated diabatic heating in Fig. 12b is near
 626 zero for the cumulus fluxes, positive for the precipitation contribution, and negative for the
 627 radiatively-driven contribution.

628 **5.2 The mesoscale moisture budget equation and humidity self-aggregation**

629 In this section, we derive a mesoscale block-averaged humidity budget equation. We
 630 block-average (square brackets) the perturbation equation (12) for q_t :

$$631 \quad \frac{\partial q_{tm}}{\partial t} = - \left[\mathbf{u}_h \cdot \nabla_h q'_t + w \frac{\partial q'_t}{\partial z} \right]_m - w_m \frac{d\bar{q}_t}{dz} + S_{qtm}. \quad (27)$$

632 Although we can't make WTG-like simplifying approximations, we can still make the
 633 scale separation argument that

$$634 \quad [\nabla_h \cdot (\mathbf{u}_{hc} q_{tc})]_m \ll \frac{1}{\rho_0} \frac{\partial}{\partial z} [\rho_0 w_c q_{tc}]_m = \frac{1}{\rho_0} \frac{\partial}{\partial z} F_{qtm}^{Cu}. \quad (28)$$

Thus,

$$\begin{aligned}
\left[\mathbf{u}_h \cdot \nabla_h q'_t + w \frac{\partial q'_t}{\partial z} \right]_m &= [\mathbf{u} \cdot \nabla q'_t]_m \\
&= \frac{1}{\rho_0} [\nabla \cdot (\rho_0 \mathbf{u} q'_t)]_m \\
&= \frac{1}{\rho_0} [\nabla \cdot (\rho_0 (\bar{\mathbf{u}} + \mathbf{u}_m + \mathbf{u}_c)(q_{tm} + q_{tc}))]_m \\
&= \frac{1}{\rho_0} [\nabla \cdot (\rho_0 ((\bar{\mathbf{u}} + \mathbf{u}_m) q_{tm} + \mathbf{u}_c q_{tc}))]_m \\
&= (\bar{\mathbf{u}} + \mathbf{u}_m) \cdot \nabla q_{tm} + [\nabla_h \cdot (\mathbf{u}_{hc} q_{tc})]_m + \frac{1}{\rho_0} \frac{\partial}{\partial z} [\rho_0 w_c q_{tc}]_m \\
&\approx (\bar{\mathbf{u}} + \mathbf{u}_m) \cdot \nabla q_{tm} + \frac{1}{\rho_0} \frac{\partial}{\partial z} F_{qtm}^{Cu}.
\end{aligned} \tag{29}$$

From (3) the block-averaged humidity source term is

$$S_{qtm} = \frac{1}{\rho_0} \frac{\partial P_m}{\partial z}. \tag{30}$$

Substituting (29) and (30) into the block-averaged humidity equation (27), we obtain

$$\frac{\partial q_{tm}}{\partial t} = C_m + A_m \tag{31}$$

The first term

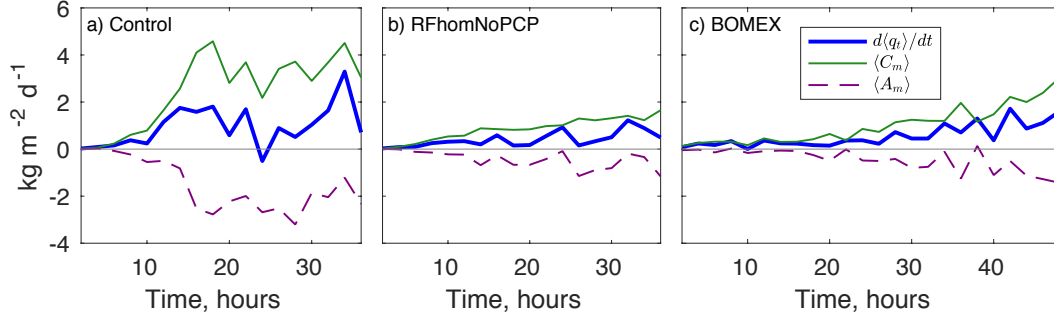
$$C_m = \frac{1}{\rho_0} \frac{\partial}{\partial z} (P - F_{qt}^{Cu})_m - w_m \frac{d\bar{q}_t}{dz}, \tag{32}$$

which Chikira [2014] named the ‘column process’, is the combined moistening effect of the moist processes and diabatically-induced vertical advection across the horizontal-mean moisture gradient. The second term

$$A_m = -(\bar{\mathbf{u}} + \mathbf{u}_m) \cdot \nabla q_{tm} \tag{33}$$

is due to advection of mesoscale moisture anomalies.

Fig. 13 shows time series of the column-integrated $\langle C_m \rangle$ and $\langle A_m \rangle$ averaged over the moistest quartile of blocks for the control and the two minimal-physics sensitivity simulations, along with their sum, the column moisture tendency. In all three cases, there is almost always net moisture storage in these moist blocks, amplifying their moisture anomalies. The column process generally moistens, and the moisture anomaly advection dries the columns. Early in the aggregation process (up through 12 hours) $\langle C_m \rangle$ typically exceeds $\langle A_m \rangle$ by a factor of two, and for the BOMEX simulation this continues throughout the 48-hour period shown. Thus the column process is the main driver of the development of moisture self-aggregation, and $\langle C_m \rangle > 0$ appears to a necessary (though perhaps not sufficient) condition for moisture self-aggregation in this setting.



663 **Figure 13.** Time series of selected components of the moistest-quartile column-integrated moisture bud-
 664 get in the (a) control, (b) RFhomNoPCP and (c) BOMEX simulations. Shown are the moistening due to the
 665 column process, advection of mesoscale perturbations and q_t storage.

666 5.3 MSE budget view of the column process feedback on the humidity budget

667 A useful way to analyze the column process moistening tendency is to rephrase it in
 668 terms of moist static energy (MSE) $h = c_p T + L_v q_v + gz = s_l + L_v q_t$, which has the
 669 advantage of not being directly affected by liquid precipitation. From (5),

$$670 \quad h = s_{vl} + \mu L_v q_t. \quad (34)$$

671 Applying the WTG approximation $s_{vlm} \approx 0$, this equation implies that mesoscale MSE
 672 anomalies are proportional to the humidity anomalies:

$$673 \quad h_m \approx \mu L_v q_{tm}. \quad (35)$$

674 Similarly, adding the s_{vl} equation (20) to μL_v times the equation (32) defining the column
 675 process,

$$676 \quad \mu L_v C_m = -w_m \frac{d\bar{h}}{dz} - \frac{1}{\rho_0} \frac{\partial}{\partial z} (F_R + F_h^{Cu})_m, \quad (36)$$

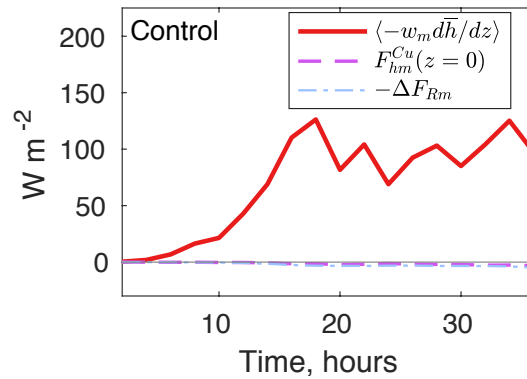
$$677 \quad \mu L_v \langle C_m \rangle = -\langle w_m \frac{\partial \bar{h}}{\partial z} \rangle + F_{hm}^{Cu}(z=0) - \Delta F_{Rm}. \quad (37)$$

678 This decomposition of $\langle C_m \rangle$ naturally arises from constructing a block-average column
 679 MSE budget, as used in the study of deep convective self-aggregation [Bretherton *et al.*,
 680 2005].

681 Fig. 14 shows time series of the terms of (37) averaged over the moistest quartile of
 682 blocks in the control run. The vertical advection term is positive and dominates the sur-
 683 face flux and radiation terms. In the vocabulary of deep convective organization [Raymond
 684 *et al.*, 2009], this is called negative gross moist stability [Yu *et al.*, 1998], i. e. mesoscale

685 circulations acting on the horizontal-mean thermodynamic profiles converge MSE into
 686 columns with already high MSE.

687 The sign of this vertical advection term for shallow convection is driven by the de-
 688 crease of domain-mean MSE $\bar{h}(z)$ with height, coupled to the structure of the mesoscale
 689 vertical motions driven by the apparent heating. Anomalous mesoscale ascent in the cu-
 690 mulus layer of the moist regions drives a positive contribution to $\langle C_m \rangle$, while the descent
 691 in the inversion layer drives a negative contribution. Even without precipitation, the posi-
 692 tive contribution outweighs the negative, as argued in Section 6. As precipitation increases
 693 within moist columns, the associated net latent heating enhances the upward motions in
 694 the cumulus layer and diminishes the evaporatively-driven downward motions in the inver-
 695 sion layer, further increasing the gross moist instability.



696 **Figure 14.** Time series of the contributions to moist-quartile column moistening $\langle C_m \rangle$ from vertical MSE
 697 advection, anomalous surface fluxes, and anomalous column radiative heating.

698 Fig. 14 also shows that the anomalous column radiative heating $-\Delta F_{Rm}$ is slightly
 699 negative in anomalously moist columns, apparently acting to counter self-aggregation. The
 700 extra cloud and water vapor in the moist columns enhance boundary-layer radiative cool-
 701 ing. The anomalous surface flux $F_{hm}^{Cu}(z=0)$ is also small and slightly negative in moist
 702 columns. Both of these results are opposite to the initial stages of deep convective self-
 703 aggregation, in which extensive anvil cirrus clouds and vigorous cold pools decrease ra-
 704 diative cooling and increase surface fluxes in moist columns (*Bretherton et al. [2005]*).
 705 From the column MSE budget perspective, shallow convective self-aggregation is funda-
 706 mentally driven by mesoscale advective feedbacks, while deep convective self-aggregation
 707 is driven by radiative and surface flux feedbacks.

708 Following *Chikira* [2014], one could also process-partition the column process moist-
 709 ening tendency by separating the contribution to mesoscale vertical motions from heat-
 710 ing by different physical processes (e. g. cumulus fluxes, precipitation, radiation) that can
 711 be added to the direct moistening contribution from those processes. Although this ap-
 712 proach is attractive in principle, and useful in special cases (see Sec. 6) it did not lead us
 713 to additional general insights about our simulations because the cumulus fluxes, radiative
 714 heating and precipitation are highly interdependent. For instance, the RFhom sensitivity
 715 study suggests that allowing horizontally inhomogeneous radiative heating speeds up self-
 716 aggregation. However, the anomalous radiative heating leads to a negative contribution
 717 $-\Delta F_{Rm}$ to the anomalous column MSE tendency in moist columns. That extra radiative
 718 cooling also induces mesoscale downward motion, producing an additional advective MSE
 719 sink (not shown). Thus, according to the budget approach, both the direct and circulation-
 720 induced radiative contributions appear to disfavor self-aggregation. This apparent contra-
 721 diction can be resolved by recognizing that anomalous radiative cooling in the inversion
 722 layer destabilizes the underlying boundary layer and stimulates more cumulus convection
 723 in moist columns, which acts as a MSE source. This illustrates the limitations of budget
 724 approaches to predicting how a complex interconnected system will respond to changed
 725 conditions.

726 **5.4 What limits the amplitude of self-aggregation?**

727 In our simulations, self-aggregation of TWP tends to slow down once the quartile
 728 TWP anomalies reach 5–10% of the domain-mean TWP. Our budget analysis suggests that
 729 as humidity aggregation intensifies, these moisture anomalies increasingly get advected out
 730 of the moist regions, as encapsulated in the term $\langle A_m \rangle$ in the moisture budget (31). Using
 731 (33), this term can be broken down:

$$732 \quad \langle A_m \rangle = -\langle \bar{\mathbf{u}}_h \cdot \nabla_h q_{tm} \rangle - \langle \bar{w} \partial q_{tm} / \partial z \rangle - \langle \bar{\mathbf{u}}_m \cdot \nabla q_{tm} \rangle \quad (38)$$

733 We ran our LES in an reference frame moving with approximately the mean boundary-
 734 layer wind, as noted in Section 2.3. This is advantageous for moisture budget analysis, be-
 735 cause otherwise the boundary-layer mean wind would rapidly advect mesoscale anomalies
 736 between subdomains.

737 In such a reference frame, the three terms all tend to damp mesoscale humidity
 738 anomalies. The first term, the horizontal advection of q_{tm} by a vertically-varying mean

739 wind, can shear out moisture anomalies. The second term, due to mean subsidence, damps
 740 mesoscale humidity perturbations by squashing them toward the surface on a divergence
 741 timescale. The third term, advection by mesoscale circulations, horizontally mixes the
 742 anomalously moist and dry regions. It becomes increasingly effective as the moisture
 743 anomalies and mesoscale circulations strengthen.

744 **6 Mesoscale humidity aggregation in the minimal-physics case**

745 We now consider what the mesoscale column moisture budget, together with WTG,
 746 implies about the development of mesoscale humidity aggregation in the minimal-physics
 747 case of no precipitation and no mesoscale variation of radiation or surface fluxes, since
 748 our sensitivity tests shows that these restrictions do not prevent aggregation in the S6 and
 749 BOMEX cases.

750 **6.1 Importance of a concave $\bar{h} - \bar{s}_{vl}$ curve**

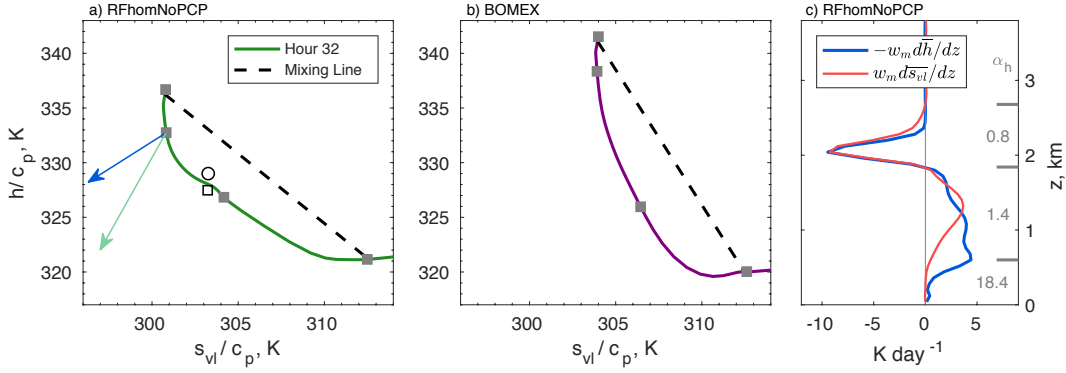
751 In the minimal-physics case, the source terms in the budgets for mesoscale anoma-
 752 lies of s_{vl} , q_t and h due to mesoscale anomalies of precipitation, radiation and surface
 753 fluxes all vanish. The column moistening due to the column process is entirely due to
 754 mesoscale advection across the mean vertical gradients induced by apparent heating from
 755 the cumulus fluxes:

$$756 \quad \langle C_m \rangle = -\langle w_m d\bar{h}/dz \rangle. \quad (39)$$

757 In the minimal-physics case the mesoscale anomaly in the apparent heating profile,
 758 defined in Eq. (21), is due only to the convergence of the anomalous cumulus s_{vl} flux.
 759 This is positive in the cumulus layer due to updraft condensational heating, and negative
 760 in the inversion layer due to evaporative cooling. However, since we assume no mesoscale
 761 anomalies of the s_{vl} flux in the minimal-physics case, the anomalous s_{vl} flux has a zero
 762 vertical integral. The vertical integral of Eq. (21) then implies that

$$763 \quad 0 = \langle w_m d\bar{s}_{vl}/dz \rangle. \quad (40)$$

764 Comparing Eqs. (39) and (40), were there a ‘mixing line’ relationship between $\bar{h}(z)$ and
 765 $\bar{s}_{vl}(z)$, or equivalently, between $\bar{q}_t(z)$ and $\bar{s}_{vl}(z)$, their vertical gradients would be linearly
 766 proportional and the column moistening due to the cumulus convection would be zero.



767 **Figure 15.** Plot of $\bar{h}(z)$ vs. $\bar{s}_{vl}(z)$ at 32 hours, in the (a) RFhomNoPCP and (b) BOMEX simulations. The
 768 grey squares indicate the surface, cumulus base, inversion base and inversion top. For RFhomNoPCP, these
 769 correspond to $z \approx 0, 0.6, 1.8, 2.7$ km. A black dashed mixing line is shown between the surface grid level
 770 and the inversion top. In (a), the arrows indicate how radiative cooling (blue) and cold advection (light green)
 771 pull the \bar{h} - \bar{s}_{vl} curve away from the mixing line, while the black circle and square in (a) show the moist (Q4)
 772 and dry (Q1) quartile means at 1.5 km altitude. Panel (c) shows the moist-quartile profiles of the mesoscale
 773 vertical advective cooling (red) and MSE source (blue) for RFhomNoPCP, and average values of the Chikira
 774 parameter α_h for the subcloud, cumulus, and inversion layers.

775 However, Fig. 15a-b shows that for the thermodynamic profiles that we have been
 776 simulating in our two minimal-physics cases, $\bar{h}(z)$ is a generally concave function of $\bar{s}_{vl}(z)$.
 777 Following *Chikira* [2014], we define a nondimensional measure of the vertical MSE gradi-
 778 ent to the dry stratification:

$$779 \alpha_h(z, t) = -\frac{d\bar{h}/dz}{d\bar{s}_{vl}/dz}. \quad (41)$$

780 This is the negative slope of the $\bar{h}(z)$ - $\bar{s}_{vl}(z)$ curve, which can easily be visualized from
 781 Fig. 15a-b. A concave $\bar{h}(z)$ - $\bar{s}_{vl}(z)$ curve is equivalent to α_h decreasing with $\bar{s}_{vl}(z)$ and
 782 thus with height. In both minimal-physics cases, α_h decreases from nearly infinity in the
 783 subcloud layer to near zero near the inversion top.

784 Fig. 15c shows the vertical profiles of $-w_m d\bar{h}/dz$ and $w_m d\bar{s}_{vl}/dz$ for RFhomNoPCP
 785 at 32 hrs. At each height, their ratio is $\alpha_h(z)$. Consistent with the $\bar{h}(z)$ - $\bar{s}_{vl}(z)$ curve,
 786 $-w_m d\bar{h}/dz$ is much larger than $w_m d\bar{s}_{vl}/dz$ in the subcloud and lower cumulus layer.
 787 Above this level, they are comparable, except near the inversion top, where $-w_m d\bar{h}/dz$ be-
 788 comes smaller than $w_m d\bar{s}_{vl}/dz$. On the right of Fig. 15c are layer-mean values of $\alpha_h(z, t)$
 789 calculated as ratios of the layer integrals of the plotted curves for the sub-cloud, sub-
 790 inversion cumulus and inversion layers. The subcloud-mean α_h exceeds 18. Averaged be-

791 tween the cumulus cloud base and the inversion, α_h is 1.4, while in the inversion layer α_h
792 is only 0.8.

793 Comparing these profiles, the general decrease of α_h with height is exactly what is
794 needed to make the vertical integral $\langle w_m d\bar{h}/dz \rangle$ positive, even though the vertical integral
795 $\langle w_m d\bar{s}_{vl}/dz \rangle$ is zero. Indeed, following *Chikira* [2014] the mesoscale advective feedback
796 term can be written as a weighted average of the apparent heating rate using WTG, as ex-
797 pressed in (21):

$$798 \quad -\langle w_m \frac{\partial \bar{h}}{\partial z} \rangle = \langle \alpha_h S_{svlm}^{app} \rangle. \quad (42)$$

799 For the minimal-physics case, there is a positive lobe of S_{svlm}^{app} low in the boundary layer,
800 where α_h is large, and a negative lobe of equal vertical integral in the inversion layer,
801 where α_h is small. This ensures that the weighted average $\langle \alpha_h S_{svlm}^{app} \rangle > 0$, i. e. nega-
802 tive gross moist stability and positive moisture convergence into moist columns from the
803 mesoscale advection contribution to the column process.

804 The inclusion of shallow cumulus precipitation would amplify the positive lobe and
805 diminish the negative lobe of $\langle S_{svlm}^{app} \rangle$. As long as \bar{h} is a decreasing function of height (so
806 $\alpha_h > 0$) through the shallow cumulus layer, this will help make $\langle \alpha_h S_{svlm}^{app} \rangle$ positive and
807 strengthen the convergence feedback on amplifying mesoscale moisture anomalies.

808 **6.2 Origin of a concave $\bar{h} - \bar{s}_{vl}$ curve**

809 Pure turbulent and convective mixing would establish vertical profiles of $\bar{h}(z)$ vs.
810 $\bar{s}_{vl}(z)$ that would trace out a mixing line on the $\bar{h}(z) - \bar{s}_{vl}(z)$ plot, with end points corre-
811 sponding to air from the subcloud layer and the free troposphere just above the inversion
812 top. In Fig. 15a-b, this mixing line is indicated by black dashes.

813 A concave $\bar{h}(z) - \bar{s}_{vl}(z)$ curve and the associated decrease of $\alpha_h(z)$ with height can
814 be maintained in typical cloud-topped boundary layers by a combination of radiative cool-
815 ing and cold advection. Mean boundary-layer radiative cooling reduces the s_{vl} of boundary-
816 layer air without affecting its q_t , pulling the $\bar{h}(z) - \bar{s}_{vl}(z)$ curve leftward and downward be-
817 tween the end points of the mixing line to create a concave shape, as shown by the blue
818 arrow in Fig. 15a. Horizontal advection of cold, dry air reduces both the s_{vl} and q_t of
819 boundary-layer air, pulling the curve to the left and even more strongly downward (light
820 green arrow in Fig. 15a) to add to its concavity. The effect of these processes in creat-
821 ing deviations from a mixing line is larger in a shallow cumulus boundary layer, where

822 the turnover timescale in the cumulus layer and especially the inversion layer is many
 823 hours, than in a well-mixed stratocumulus-capped boundary layer with a much shorter
 824 eddy turnover time [Bretherton *et al.*, 1995].

825 It is interesting to consider how the horizontal mesoscale temperature-humidity vari-
 826 ability in the schematic of Fig. 10 fits into this description. At a given altitude, e. g. the
 827 inversion base, s_{vl} is constant while q_t and hence h varies between the dry and moist re-
 828 gions. This structure would trace out a vertical line in the h - s_{vl} plot. The open square
 829 and circle in Fig. 15a shows the points on this plot corresponding to the dry (Q1) and
 830 moist (Q4) quartiles at 1.5 km altitude at 32 hrs. As expected, the moist-quartile point
 831 lies above the dry-quartile plot, and is thus closer to the mixing line, reflecting the more
 832 vigorous vertical mixing in the active cumulus convection of the moist regions.

833 A peculiarity visible in Fig. 15a is a slight reversal in the $\bar{h}(z)$ - $\bar{s}_{vl}(z)$ concavity aris-
 834 ing from elevations between 1.5-2 km. This is a layer that is actually above the inversion
 835 base in the ECMWF summertime climatological profile from which this case was derived.
 836 Because the inversion in this region slopes down toward the east (the upwind direction),
 837 there is horizontal advective warming and drying at this level, rather than the cooling and
 838 moistening characteristic of the interior of the boundary layer. This advective forcing pulls
 839 the $\bar{h}(z)$ - $\bar{s}_{vl}(z)$ slightly up and right in that layer. Because the simulated boundary layer
 840 is somewhat deeper than that in the ECMWF climatology, that feature is artificially moved
 841 down into its interior.

842 **6.3 Relation to the theory of entrainment-related mesoscale production of humid-** 843 **ity variance**

844 In the Introduction, we suggested that our analysis is related to the theory of entrainment-
 845 induced mesoscale production of humidity variance outlined by Jonker *et al.* [1999] and
 846 DeRoode *et al.* [2004]. One connection is formal. The question of whether moist blocks
 847 get moister is similar to asking whether the domain-mean mesoscale humidity variance in-
 848 creases. Formally, one could multiply our equation (27) for the tendency dq_{tm}/dt by $2q_{tm}$
 849 and horizontally average across all the blocks to get an equation for the tendency of the
 850 mesoscale humidity variance $\overline{q_{tm}^2}$. As discussed above, a critical term on the right hand
 851 of (27) is $-w_m d\bar{q}_t/dz$; its contribution to the mesoscale humidity variance tendency is
 852 $-2q_m w_m d\bar{q}_t/dz$, consistent with the variance budget equation in DeRoode *et al.* [2004].

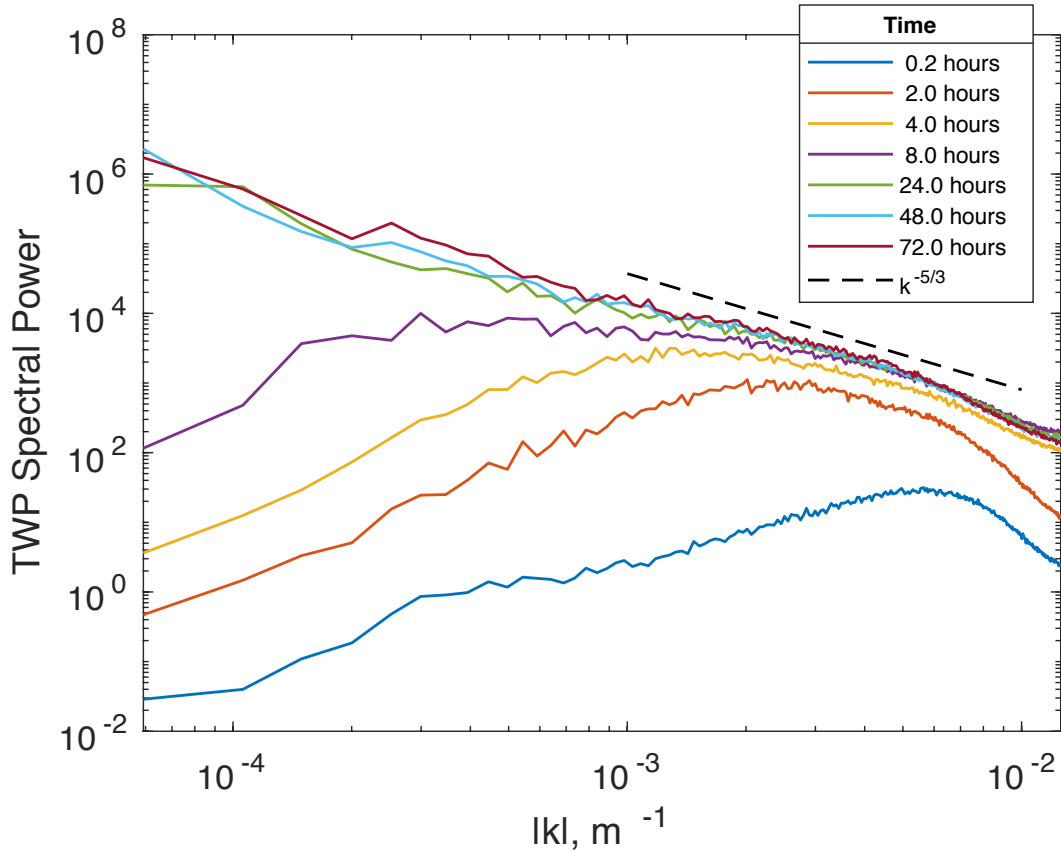
853 A second related connection is the finding of *Jonker et al.* [1999] that in a dry con-
 854 vective boundary layer, only scalars that are not linearly related to the virtual potential
 855 temperature undergo mesoscale variance growth. *DeRoode et al.* [2004] found analogous
 856 results for stratocumulus-like mixed layers. For our minimal-physics case, we found that
 857 in a shallow cumulus boundary layer, growth of column q_{tm} variance won't occur if \bar{q}_t
 858 is a linear function of \bar{s}_{vl} , which is our analogue to virtual potential temperature. Al-
 859 though the vertical structures of \bar{q}_t and \bar{s}_{vl} are vastly different between a dry convective
 860 or stratocumulus-capped mixed layer, these results both can be traced to the conditions
 861 needed to obtain positive mesoscale variance production of humidity in a fluid which can-
 862 not support large horizontal variations in density.

863 Fourier spectra of total water path from our control simulation (Fig. 16) show a
 864 long-wavelength tail analogous to similar spectra from LES of closed-cell convection, e. g.
 865 Fig. 4 of *Schroeter et al.* [2005], with steady growth of power at low wavenumbers that
 866 saturates into a behavior not far from an $O(|k|^{-5/3})$ power-law; the saturation takes longer
 867 for lower wavenumbers and is complete after 24 hours, with little further spectral change
 868 out to 72 hours. A qualitatively similar evolution is even seen in the Fourier spectrum of
 869 a passive scalar in a dry convective boundary layer [*Jonker et al.*, 1999]. However, in a
 870 moist boundary layer, unlike a dry convective boundary layer, humidity is not a passive
 871 scalar but leads to clouds which can cause latent and radiative heating that feed back on
 872 the mesoscale circulations, which in turn help amplify the mesoscale humidity variance.

875 7 Discussion and Conclusions

876 Large-domain (128 km)² large-eddy simulations of northeastern Pacific shallow cu-
 877 mulus convection spontaneously and robustly develop mesoscale humidity and cloud ag-
 878 gregation within 1–3 days, even if precipitation or mesoscale radiative and surface flux
 879 feedbacks are suppressed.

880 We used the weak temperature gradient approximation to develop a conceptual model
 881 of shallow cumulus self-aggregation as an instability of a horizontally homogeneous field
 882 of cumulus clouds in which humidity-convection feedbacks spontaneously amplify mesoscale
 883 moist and dry patches. This framing is similar to theories of deep convective self-aggregation.
 884 However, the aggregation mechanisms are different for shallow vs. deep convection be-
 885 cause of their different vertical structures of the mesoscale vertical velocity and moist



873 **Figure 16.** Spectrum of total water path vs. magnitude $|k|$ of horizontal two-dimensional wavenumber at a
 874 sequence of times in the control simulation.

886 static energy profiles. Deep convection requires mesoscale radiative feedback to aggregate.
 887 The associated vertical circulations have positive gross moist stability, i.e., in the net
 888 they diverge MSE out of moist, high MSE, columns, opposing and slowing the aggregation
 889 process. Shallow convection aggregates quickly through a purely dynamical mechanism
 890 because it has negative gross moist stability; the mesoscale vertical motions and
 891 MSE profile are configured so as to converge MSE into moist columns. We argued that in
 892 the simplest case of nonprecipitating cumulus clouds, this negative gross moist stability is
 893 due to the mean radiative cooling of the boundary layer.

894 As the cumuli in moist regions precipitate more, driving mesoscale ascent with
 895 their latent heating, the overlying evaporatively-driven subsidence becomes less important.
 896 With a typical tropical MSE profile, we speculate that this mesoscale vertical motion
 897 profile will keep gross moist stability negative (promoting continued aggregation) until

898 the cumulus layer deepens enough to glaciate, after which a deep-convective view of self-
899 aggregation must be adopted.

900 In Sect. 6.3, we noted connections of our analysis methods and results with ear-
901 lier work on mesoscale production of humidity variance related to entrainment of free-
902 tropospheric air into dry-convective and stratocumulus-capped mixed layers, inspired in
903 part by observations and LES of closed MCC. Further comparing the feedback mecha-
904 nisms supporting the self-aggregation of humidity and cloud in different types of cloud-
905 topped boundary layers is a worthy topic of future research.

906 Our results differ from the finding of *Seifert and Heus* [2013] that precipitation,
907 and in particular, the subcloud evaporation of precipitation, is essential to mesoscale self-
908 aggregation in the ‘moist RICO’ case they simulated. There are differences of model con-
909 figuration – the domain size for their sensitivity experiments was only 20% as large in
910 each horizontal dimension as ours, and might not support the same kind of moisture ag-
911 gregation. Their horizontal and vertical grid are also much finer; in simulations of deep
912 convective radiative-convective equilibrium, this is found to inhibit the initial develop-
913 ment of self-aggregation [*Muller and Held*, 2012]. Their microphysical parameterization
914 is different. As in our BOMEX case, the aggregation in their nonprecipitating sensitivity
915 simulation might be too slow to be obvious in the cloud field after 30 hours, even though
916 it would be clear in a simulation twice as long. Lastly, and again in contrast to *Seifert and*
917 *Heus* [2013], it is intriguing that numerical simulations of radiative-convective equilibrium
918 suggest that self-aggregation occurs in smaller domains [*Jeevanjee and Romps*, 2013] and
919 without the help of mesoscale radiative feedbacks [*Muller and Bony*, 2015] if the evapo-
920 ration of precipitation is suppressed. The aggregation mechanism in these simulations is
921 strongly connected to the development of shallow mesoscale circulations and may be qual-
922 itatively similar to the one we find in our simulations. More study of these sensitivities to
923 model, resolution, and cloud regime is warranted.

924 One foundation of the conceptual model is that the shallow cumulus clusters favor
925 mesoscale regions of higher water vapor path. A more extensive statistical analysis of
926 this correlation in satellite observations would be useful. Another aspect of this model
927 amenable to observational testing is the dipole profile of vertical velocity within the con-
928 vectively active patches.

Acknowledgments

We acknowledge support from Department of Energy ASR grant DE-SC0011602 and National Science Foundation grant AGS-1445813, and Marat Khairoutdinov for developing and managing the System for Atmospheric Modeling. Rob Wood and two anonymous referees provided constructive advice. The SAM block budget diagnostics were based on an earlier implementation by Matt Peters. The model output and Matlab scripts used to generate the analyses and figures in this paper are stored in the University of Washington ResearchWorks Archive and can be obtained at <http://hdl.handle.net/1773/39708>.

References

- Ackerman, A. S., and coauthors (2009), Large-eddy simulations of a drizzling, stratocumulus-topped marine boundary layer, *Mon. Wea. Rev.*, *137*, 1083–1110.
- Agee, E. M., T. S. Chen, and K. E. Dowell (1973), A review of mesoscale cellular convection, *Bull. Amer. Meteor. Soc.*, *54*, 1004–1012.
- Agee, E. M., and F. E. Lomax (1978), Structure of the mixed layer and inversion layer associated with patterns of mesoscale cellular convection during AMTEX 1975, *J. Atmos. Sci.*, *35*, 2281–2301.
- Berner, A. H., C. S. Bretherton, R. Wood, and A. Muhlbauer (2013), Marine boundary layer cloud regimes and POC formation in an LES coupled to a bulk aerosol scheme, *Atmos. Chem. Phys.*, *13*, 12549–12572, doi:10.5194/acp-13-12549-2013.
- Betts, A. K. (1985), Mixing line analysis of clouds and cloudy boundary layers, *J. Atmos. Sci.*, *42*, 2751–2763.
- Blossey, P. N., C. S. Bretherton, and M. C. Wyant, (2009), Understanding subtropical low cloud response to a warmer climate in a superparameterized climate model. Part II: Column modeling with a cloud-resolving model, *J. Adv. Model Earth Syst.*, *1*, 8, doi:10.3894/JAMES.2009.1.8.
- Blossey, P. N., C. S. Bretherton, M. Zhang, A. Cheng, S. Endo, T. Heus, Y. Liu, A. Lock, S. R. de Roode and K.-M. Xu (2013), Marine low cloud sensitivity to an idealized climate change: The CGILS LES intercomparison, *J. Adv. Model. Earth Syst.*, *5*, 234–258, doi:10.1002/jame.20025.
- Bretherton, C. S., and P. K. Smolarkiewicz (1989), Gravity waves, compensating subsidence and detrainment around cumulus clouds, *J. Atmos. Sci.*, *46*, 740–759.

- 960 Bretherton, C. S., and M. C. Wyant (1997), Moisture transport, lower tropospheric stabil-
 961 ity and decoupling of cloud-topped boundary layers, *J. Atmos. Sci.*, *54*, 148–167.
- 962 Bretherton, C. S., P. Austin, and S. T. Siems (1995), Cloudiness and marine boundary
 963 layer dynamics in the ASTEX Lagrangian experiments. Part II: Cloudiness, drizzle, sur-
 964 face fluxes and entrainment, *J. Atmos. Sci.*, *52*, 2724–2735.
- 965 Bretherton, C. S., P. N. Blossey, and M. Khairoutdinov (2005), An energy-balance analysis
 966 of deep convective self-aggregation above uniform SST, *J. Atmos. Sci.*, *62*, 4273–4292.
- 967 Chikira, M. (2014), Eastward-propagating intraseasonal oscillation represented by Chikira-
 968 Sugiyama cumulus parameterization. Part II: Understanding moisture variation under
 969 weak temperature gradient balance, *J. Atmos. Sci.*, *71*, 615–639, doi:10.1175/JAS-D-13-
 970 038.1.
- 971 De Roode, S. R., P. G. Duynkerke, and H. M. M. Jonker (2004), Large-eddy simulation:
 972 How large is large enough? *J. Atmos. Sci.*, *64*, 403–421.
- 973 Emanuel, K., A. A. Wing, and E. M. Vincent (2014), Radiative-convective instability, *J.*
 974 *Adv. Model. Earth Syst.*, *6*, 75–90, doi:10.1002/2013MS000270.
- 975 Fiedler, B. H. (1984), The mesoscale stability of entrainment into cloud-topped mixed lay-
 976 ers. *J. Atmos. Sci.*, *41*, 92–101.
- 977 Geoffroy, O., J.-L. Brenguier, and F. Burnet (2010), Parametric representation of the cloud
 978 droplet spectra for LES warm bulk microphysical schemes, *Atmos. Chem. Phys.*, *10*,
 979 4835–4848, doi:10.5194/acp-10-4835-2010.
- 980 Held, I. M., R. S. Hemler, and V. Ramaswamy (1993), Radiative-convective equilibrium
 981 with explicit two-dimensional convection, *J. Atmos. Sci.*, *50*, 3909–3927.
- 982 Jeevanjee, N., and D. M. Romps (2013), Convective self-aggregation, cold pools, and do-
 983 main size, *Geophys. Res. Lett.*, *40*, 994D998, doi:10.1002/grl.50204.
- 984 Johnson, R. H., and M. E. Nicholls (1983), A composite analysis of the boundary layer
 985 accompanying a tropical squall line, *Mon. Wea. Rev.*, *111*, 308–319.
- 986 Jonker, H. J. J., P. G. Duynkerke, and J. W. M. Cuijpers (1999), Mesoscale fluctuations in
 987 scalars generated by boundary layer convection, *J. Atmos. Sci.*, *56*, 801–808.
- 988 Kazil, J., T. Yamaguchi, and G. Feingold (2017), Mesoscale organization, entrainment,
 989 and the properties of a closed-cell stratocumulus cloud, *J. Adv. Model. Earth Syst.*, *9*,
 990 doi:10.1002/2017MS001072.
- 991 Khairoutdinov, M. F. and Y. L. Kogan (2000), A new cloud physics parameterization in a
 992 large-eddy simulation model of marine stratocumulus, *Mon. Wea. Rev.*, *128*, 229–243.

- 993 Khairoutdinov, M. F., and D. A. Randall (2003), Cloud resolving modeling of the ARM
994 Summer 1997 IOP: Model formulation, results, uncertainties, and sensitivities, *J. Atmos.*
995 *Sci.*, *60*, 607–625.
- 996 LeMone, M. A., and R. J. Meitin (1984), Three examples of fair-weather mesoscale
997 boundary layer convection in the tropics, *Mon. Wea. Rev.*, *112*, 1985–1997.
- 998 Malkus, J. S., and H. Riehl (1964), *Cloud Structure and Distribution over the Tropical Pa-*
999 *cific Ocean*, University of California Press, 229 pp.
- 1000 Mlawer, E. J., S. J. Taubman, P. D. Brown, M. J. Iacono, and S. A. Clough (1997),
1001 RRTM, a validated correlated-k model for the longwave, *J. Geophys. Res.*, *102*, 663–
1002 682, doi:10.1029/97JD00237
- 1003 Morrison, H., J. A. Curry, and V. I. Khvorostyanov (2005), A new double-moment micro-
1004 physics parameterization for application in cloud and climate models. Part I: Descrip-
1005 tion, *J. Atmos. Sci.*, *62*, 1665–1677, doi:10.1175/JAS3446.1.
- 1006 Mueller, G., and A. Chlond (1996), Three-dimensional numerical study of cell broadening
1007 during cold air outbreaks, *Bound.-Layer Meteor.*, *81*, 289–323.
- 1008 Muller, C., and S. Bony (2015), What favors convective aggregation and why?, *Geophys.*
1009 *Res. Lett.*, *42*, 5626–5634, doi:10.1002/2015GL064260.
- 1010 Muller, C. J., and I. M. Held (2012), Detailed investigation of the self-aggregation of con-
1011 vection in cloud resolving simulations, *J. Atmos. Sci.*, *69*, 2551–2565, doi:10.1175/JAS-
1012 D-11-0257.1.
- 1013 Neale, R. B. and coauthors (2012), *Description of the NCAR Community Atmosphere Model*
1014 *(CAM 5.0)*, NCAR Technical Note NCAR/TN-486+STR, 273 pp.
- 1015 Nuijens, L, I. Serikov, L. Hirsch, K. Lonitz and B. Stevens (2014), The distribution and
1016 variability of low-level cloud in the North Atlantic trades, *Q. J. R. Meteorol. Soc.*, *140*,
1017 2364–2374, doi:10.1002/qj.2307.
- 1018 Raymond, D. J., S. L. Sessions, A. H. Sobel, and Ž. Fuchs (2009), The mechanics of
1019 gross moist stability, *J. Adv. Model. Earth Syst.*, *1*, 9, doi:10.3894/JAMES.2009.1.9.
- 1020 Rothermel, J. and E. M. Agee (1980), Aircraft investigation of mesoscale cellular convec-
1021 tion during AMTEX 1975, *J. Atmos. Sci.*, *37*, 1027–1040.
- 1022 Schroeter, M., S. Raasch, and H. Jansen (2005), Cell broadening revisited: Results from
1023 high-resolution large-eddy simulations of cold air outbreaks, *J. Atmos. Sci.*, *62*, 2023–
1024 2032, doi:10.1175/JAS3451.1.

- 1025 Seifert, A., and T. Heus (2013), Large-eddy simulation of organized precipitating trade
1026 wind cumulus clouds, *Atmos. Chem. Phys.*, *13*, 5631–5645, doi:10.5194/acp-13-5631-
1027 2013.
- 1028 Seifert, A., T. Heus, R. Pincus and B. Stevens (2015), Large-eddy simulation of the tran-
1029 sient and near-equilibrium behavior of precipitating shallow convection, *J. Adv. Model.*
1030 *Earth Syst.*, *7*, 1918–1937, doi:10.1002/2015MS000489.
- 1031 Siebesma, A. P., and coauthors (2003), A large-eddy simulation intercomparison study of
1032 shallow cumulus convection, *J. Atmos. Sci.*, *60*, 1201-1219.
- 1033 Sobel, A., and C. Bretherton (2000), Modeling tropical precipitation in a single column, *J.*
1034 *Climate.*, *13*, 4378–4392.
- 1035 Tobin, I., S. Bony, and R. Roca (2012), Observational evidence for relationships between
1036 the degree of aggregation of deep convection, water vapor, surface fluxes, and radiation,
1037 *J. Climate*, *25*, 6885–6904.
- 1038 Tompkins, A. M. (2001), Organization of tropical convection in low vertical wind shears:
1039 The role of water vapor, *J. Atmos. Sci.*, *58*, 529–545.
- 1040 Vogel, R., L. Nuijens, and B. Stevens (2016), The role of precipitation and spatial organ-
1041 ization in the response of trade-wind clouds to warming, *J. Adv. Model. Earth Syst.*, *8*,
1042 843–862, doi:10.1002/2015MS000568.
- 1043 Wang, H., and G. Feingold (2009), Modeling mesoscale cellular structures and drizzle in
1044 marine stratocumulus. Part II: The microphysics and dynamics of the boundary regions
1045 between open and closed cells, *J. Atmos. Sci.*, *66*, 3257–3275.
- 1046 Wing, A.A. and K.A. Emanuel (2013), Physical mechanisms controlling self-aggregation
1047 of convection in idealized numerical modeling simulations, *J. Adv. Model. Earth Syst.*,
1048 doi: 10.1002/2013MS000269.
- 1049 Wolding, B. O., and E. D. Maloney (2015), Objective diagnostics and the Madden-Julian
1050 Oscillation. Part II: Application to moist static energy and moisture budgets, *J. Climate*,
1051 *28*, 7786–7808, doi:10.1175/JCLI-D-14-00688.1.
- 1052 Wood, R., and Hartmann, D. L. (2006), Spatial variability of liquid water path in marine
1053 low cloud: The importance of mesoscale cellular convection, *J. Climate*, *19*, 1748–1764.
- 1054 Xue, H., G. Feingold, and B. Stevens (2008), The role of precipitating cells in organizing
1055 shallow convection, *J. Atmos. Sci.*, *65*, 392–406.
- 1056 Yu, J.-Y., C. Chou, and J. D. Neelin (1998), Estimating the gross moist stability
1057 of the tropical atmosphere, *J. Atmos. Sci.*, *55*, 1354–1372, doi:10.1175/1520-

1058

0469(1998)055<1354:ETGMSO>2.0.CO;2.